Variationally consistent modeling of a sensor-actuator based on shape-morphing from electro-chemical–mechanical interactions

(article starts on next page)

Variationally consistent modeling of a sensor-actuator based on shape-morphing from electro-chemical–mechanical interactions

David Carlstedt [a,b,*], Kenneth Runesson [a], Fredrik Larsson [a], Ralf Jänicke [c], Leif E. Asp [a]

[a] *Department of Industrial and Materials Science, Chalmers University of Technology, SE 412 96, Gothenburg, Sweden*
[b] *Department of Aeronautics and Astronautics, Stanford University, CA 94305, Stanford, USA*
[c] *Institute of Applied Mechanics, Technische Universität Braunschweig, D-38106, Braunschweig, Germany*

ARTICLE INFO

ABSTRACT

This paper concerns the computational modeling of a class of carbon fiber composites, known as shape-morphing and strain-sensing composites. The actuating and sensing performance of such (smart) materials is achieved by the interplay between electrochemistry and mechanics, in particular the ability of carbon fibers to (de)intercalate Li-ions repeatedly. We focus on the actuation and sensing properties of a beam in conjunction with the appropriate "through-the-thickness" properties. Thus, the electro-chemo-mechanical analysis is essentially two-dimensional, and it is possible to rely heavily on the results in Carlstedt et al. (2020). More specifically, the cross-sectional design is composed of two electrodes, consisting of (partly) lithiated carbon fibers embedded in structural battery electrolyte (SBE), on either side of a separator. As a result, the modeling is hierarchical in the sense that (macroscale) beam action is combined with electro-chemo-mechanical interaction along the beam. The setup is able to work as sensor or actuator depending on the choice of control (and response) variables. Although quite idealized, this design allows for a qualitative investigation. In this paper we demonstrate the capability of the developed framework to simulate both the actuator and sensor modes. As proof of concept, we show that both modes of functionality can be captured using the developed framework. For the actuator mode, the predicted deformation is found to be in close agreement with experimental data. Further, the sensor-mode is found to agree with experimental data available in the literature.

1. Introduction

The class of multi-physics processes that combine electrochemistry with mechanics is essential for a variety of engineering applications. What may come first to mind is standard Li-ion batteries for which the electrochemistry modeling has a long history, e.g. the classical textbook by Newman and Thomas-Alyea (2004). Clearly, the coupling to mechanical response is important, not the least because of the detrimental impact on the electrical properties that can be caused by material damage, crack evolution and debonding at the interphases of active particle/components in the composite structure, see Xu et al. (2019), Bucci et al. (2017). In recent years, there is a growing interest in so-called "structural batteries", which combine good structural bearing capacity for applied external loading with the capability of (electrochemical) energy storage, cf. Asp et al. (2021).

Shape-morphing composites constitute yet another class of engineering materials whose performance rely on the interplay between electrochemistry and mechanics, most notably the ability to intercalate Li-ions, cf. Chin et al. (2006), Zhang and Grant

(2013). Obviously, if a structural component can change its shape significantly in a predictable and desirable fashion between several stable configurations merely from a manipulation of the Li-ion concentration in a heterogeneous fashion, one can foresee different applications as a "smart" material in sensors and actuators. Classically, the piezoelectric effect have been utilized in solids; however, to bring about significant deformations would require comparatively high electric voltage (electric potential differences). On the other hand, intercalation-based actuation can bring about more substantial actuation forces at low voltage, and it is possible to maintain the deformed shape virtually without any continuous external power supply. This property is known as zero-power hold. In a recent paper, Johannisson et al. (2020) present a novel architecture comprising commercial carbon fibers and a so-called structural battery electrolyte (SBE) that was shown to possess promising properties, most notably being able to produce large deformations at low voltage. Indeed, this type of material can be used in structural electrochemical actuators (Johannisson et al., 2020), or in structural energy harvesting and strain-sensing materials (Harnden et al., 2022; Jacques et al., 2013b; Harnden et al., 2021).

As to the modeling and consequent computational technology, the "building blocks" are not new per se; indeed, it is the combination of theory, formulation of the boundary/initial value problems, and the efficient computational solution based on the proper variational setting that can provide the desired computational tool, with which it is possible to analyze, simulate and assess a class of morphing composites. At this point it is illuminating to compare the *structural battery composite* and the *shape-morphing actuator* and *strain-sensing material*:

- The purpose of a structural battery composite is to serve as a battery, i.e. to electrochemically store and release energy as required, by transport of Li-ions. Deformations resulting in structural shape changes must be restricted or, at best, be of no relevance. An obvious way of neutralizing bending of a laminated composite is to strive for a symmetric microstructural architecture. Both potentiostatic and galvanostatic control are of interest.
- The purpose of a shape-morphing actuator is to bring about significant structural shape changes (even if strains may be small or moderate) from the "free" strain due to intercalated Li-ions. Moreover, the purpose of a strain-sensing material is to predict the mechanical strain level within the material by measuring the change in electric potentials of the lithiated carbon fiber electrodes. For simplicity (in the present paper), we consider a cantilever beam structure with zero normal force (Fig. 1a–b). We then distinguish between the "actuator" and "sensor" modes: In the "actuator mode" the beam deflection is caused by the fiber expansion/shrinkage associated with changes in Li-concentrations in the two electrodes. In the "sensor mode", however, the end displacement is prescribed (controlled). In principle, it is possible to resort to either potentiostatic or galvanostatic control in both modes. Schematic illustrations of the actuator and sensor mode for the considered cantilever beam are provided in Fig. 1a and c, and Fig. 1b and d, respectively.

Subsequently, we review briefly the literature with clear (or possible) relevance for the shape-morphing and strain-sensing composite.

First of all, it is obvious that the developments regarding Li-batteries, both conventional and structural, have a direct relevance for shape-morphing composites. Reviews of the general principles in non-equilibrium thermodynamics, as applied to electrochemo-mechanics, have been presented by Salvadori et al. (2015), and Grazioli et al. (2016). Highly localized redox reactions in the electrolyte are expected to take place in the proximity of the fiber/electrolyte interface. The classical assumption is the so-called "double-layer" approximation, and the corresponding interface relation is known as the Butler-Volmer relation, see e.g. Latz and Zausch (2013). The multiscale characteristics of porous structural electrolytes are profound. Computational homogenization has been proposed for the electrochemical–mechanical interaction in order to upscale to macroscale effective properties/variables, e.g. Salvadori et al. (2014, 2015), Zhang et al. (2020), Gupta and Gudmundson (2021), Zhuo et al. (2021).

With respect to the modeling of carbon fiber based shape-morphing composites, i.e. the type of material studied in this paper, Johannisson et al. (2020) considered a strongly simplified geometry and a simplified electrochemical process in order to adopt an analytical and a numerical model for predicting deformations due to cyclic volume change of the active materials. In terms of modeling of the strain-sensing material, Carlstedt et al. (2020) demonstrated that the voltage-strain coupling effect can be predicted by accounting for the "stress driven" part of the chemical potential. Moreover, in the work by Harnden et al. (2022), an analytical closed form solution was derived and the predicted and measured coupling effects were found to agree remarkably well. Further, it is noted that there are many examples of studies on modeling of actuators made of ionic polymer metal composites (IPMCs), see e.g. Leronni and Bardella (2021), and Cha and Porfiri (2014). However, a general modeling framework to predict the actuator and sensor functionality of the studied material, while considering the macroscale problem (beam action) in combination with the electro-chemo-mechanical interaction (microscale), is currently lacking.

As to the structural analysis of plates (and shells) with large displacements (deflections), the literature is abundant. The concept of "geometrically exact" beam and plate formulations, e.g. Simo et al. (1988), is widely used. However, in this first attempt to rigorously account for the electro-chemical–mechanical interaction, we adopt the most simple assumption of Euler–Bernoulli beam theory based on linear(ized) kinematics. The microscale features are then resolved through the cross-section of the beam, whereby it is assumed that the beam properties are completely homogeneous along its axis (for the sake of simplicity).

In this paper we extend a previously developed computational modeling framework (Carlstedt et al., 2020) to study electro-chemically driven actuators and sensors utilizing carbon fiber-SBE electrodes. The theory is applied to a beam composed of two partly lithiated carbon fiber-SBE electrodes on either side of a separator. Numerical studies are performed to demonstrate the capability of the developed framework and to simulate the actuator and sensor mode of the studied material. In accordance with previous experimental studies (Johannisson et al., 2020; Harnden et al., 2022), we start with prelithiating (or activate) the carbon fibers. Further, we perform simulations to simulate the actuator and sensor modes, and compare the numerical predictions with experimental data available in the literature (Johannisson et al., 2020; Harnden et al., 2022).
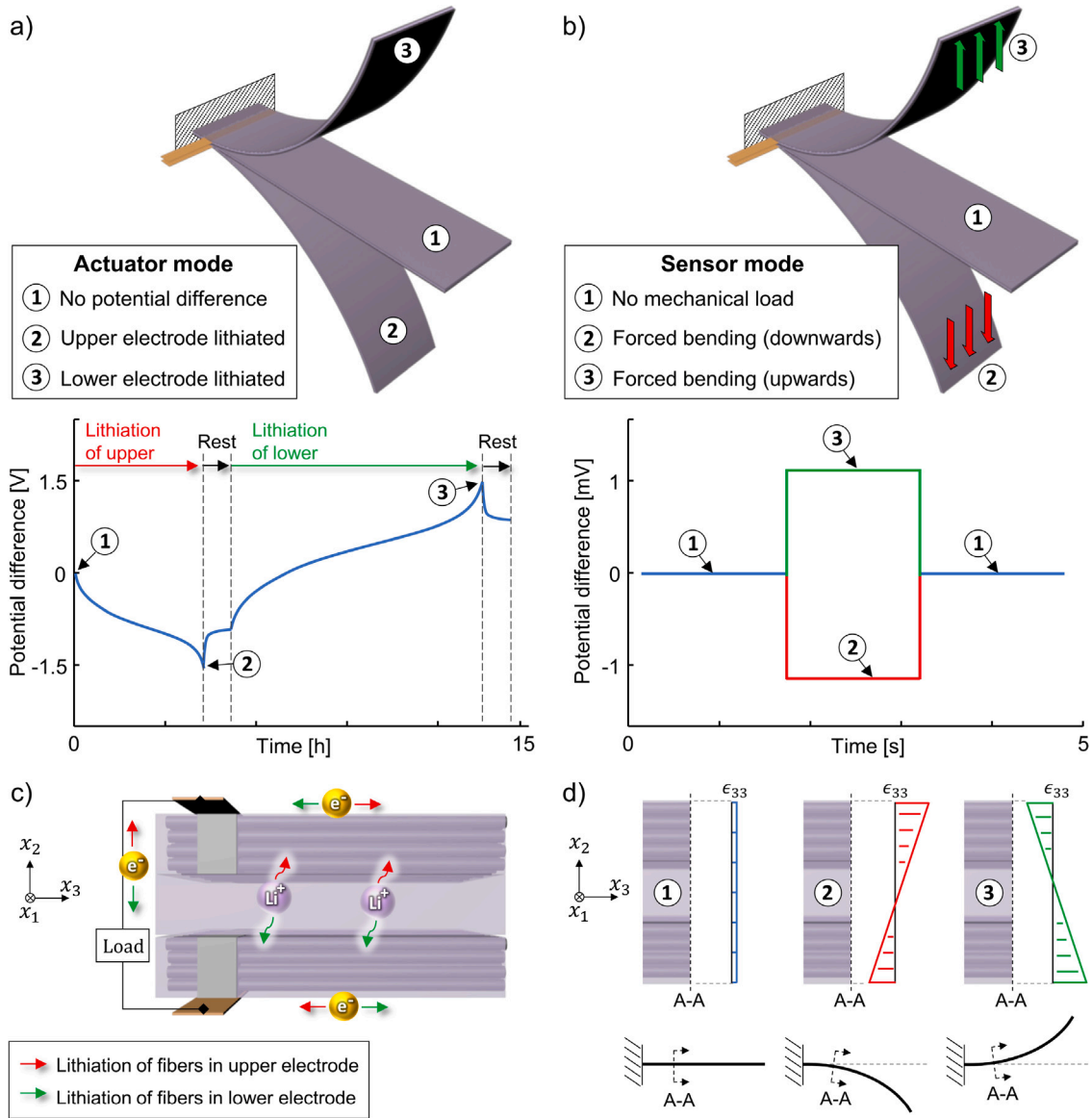
Fig. 1. (a) "Actuator mode": Structural deflection. States: (1) No potential difference between electrodes; (2) fibers in upper electrode lithiated (lower delithiated); (3) fibers in lower electrode lithiated (upper delithiated) (b) "Sensor mode": Change in electric potential. States: (1) No mechanical load; (2) Applied bending (downwards); (3) Applied bending (upwards). (c) Illustration of lithiation processes during "actuation". (d) Strain distribution in the beam cross-section for the three states.

2. Cross-sectional design

2.1. Preliminaries

To avoid unnecessary structural complexity, we consider a cantilever beam that represents the sensor/actuator functionality (cf. Fig. 1). The cross-sectional design, as proposed in Johannisson et al. (2020), Harnden et al. (2022), consists of two identical electrodes with a separator in between them. The electrodes, in their turn, are composed of partially lithiated carbon fibers that are embedded in a bicontinuous SBE (solid polymer skeleton saturated by liquid electrolyte). The separator may have a slightly more complex material architecture; however, with a similar function as the above-mentioned SBE.

The design is shown schematically in Fig. 2. More specifically, Fig. 2a (from Harnden et al. (2022)) shows a photograph of the layered design, whereas Fig. 2b gives a schematic illustration of the electrodes and the separator. Further, Fig. 2c illustrates an idealized cross-section of the beam that is used for the computational modeling. It is assumed to be doubly symmetric (also in terms of material behavior) and completely uniform along the beam axis. As to the external mechanical loading on the upper and lower
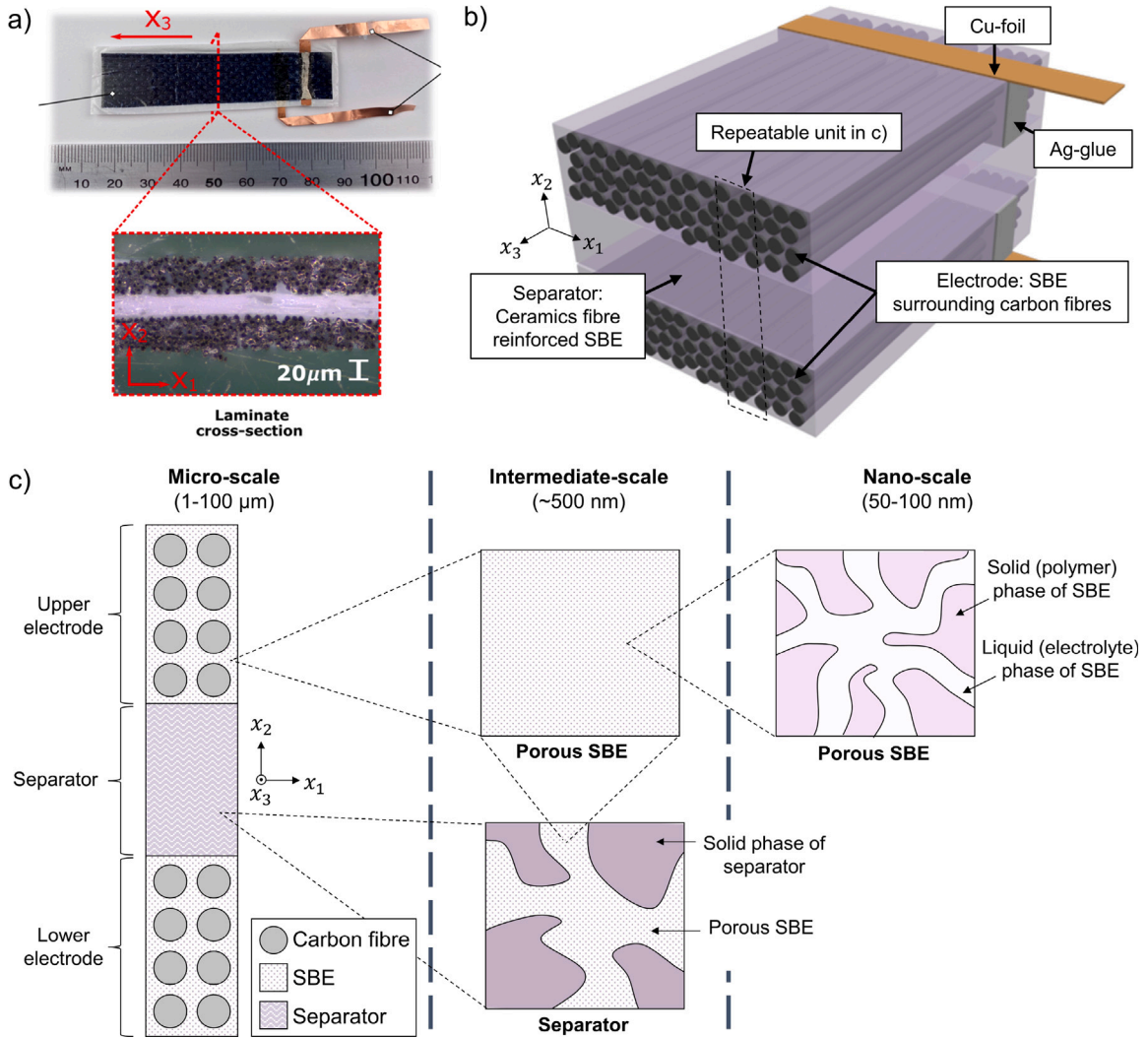
Fig. 2. Prototype carbon fiber based morphing and sensing composite. (a) Laminated cross-section. (b) Conceptual design: Separator layer sandwiched by unidirectional carbon fiber layers representing the electrodes. (c) Model design of beam cross-section, including schematic illustrations of the SBE in the electrodes and the separator domain, respectively.
Source: Reprint from Harnden et al. (2022).

surfaces, it is assumed to be symmetrical w.r.t to the vertical plane (defined by $x_1 = 0$), which means that simple bending in this plane is expected.

The idealized representation of the porous SBE and separator, including rough estimates of length scales, are presented in Fig. 2c. It should be noted that the so-called "intermediate-scale" represents a length scale between the beam cross-section at micro-scale (dimensions of unit approximately 15 x 100 μm) and the porous structure of the SBE (nano-scale, dimensions of pores approximately 100 nm), and is based on the assumed dimensions of the utilized microporous separator, cf. Arora and Zhengming (2004), Johannisson et al. (2020).

Notation: An arbitrary spatial point in the beam is represented as $\boldsymbol{x} = \hat{\boldsymbol{x}} + \bar{x}\boldsymbol{e}_3$ with $\hat{\boldsymbol{x}} := \hat{\boldsymbol{I}} \cdot \boldsymbol{x} = x_1\boldsymbol{e}_1 + x_2\boldsymbol{e}_2$, where x_1, x_2 are Cartesian coordinates in the cross-section, whereas $\bar{x}$ is the coordinate along the beam axis (located at the cross-sectional midplane), as shown in Fig. 2b. Further, $\hat{\boldsymbol{I}} := \boldsymbol{I} - \boldsymbol{e}_3 \otimes \boldsymbol{e}_3$ is the identity projection onto a cross-sectional plane. We also introduce the gradient in the cross-sectional plane as $\hat{\boldsymbol{\nabla}} := \hat{\boldsymbol{I}} \cdot \boldsymbol{\nabla} = \frac{\partial}{\partial x_1}\boldsymbol{e}_1 + \frac{\partial}{\partial x_2}\boldsymbol{e}_2$.

2.2. Electrode layers

The following special assumptions are introduced for the fiber domain(s): (i) Material properties are characterized as transversely isotropic (isotropy pertains to the cross-section); (ii) The single active species is Li, which moves into the fiber; (iii) The fibers in the two electrodes are connected via an external circuit (in which current is caused by electron transport).

The following special assumptions are introduced for the SBE: (i) Material properties are characterized as isotropic (and effective properties of the SBE are used); (ii) The Li-ions are positively charged (cation) and the companion X-ions (anion) are negatively charged; (iii) The current density is carried both by Li$^+$ and the companion anion X$^-$.

2.3. Separator layer

The separator layer consists effectively of two bicontinuous phases: One solid phase (normally a ceramic reinforced porous polymer) which is stiff and virtually electrically inactive, i.e. the ion transport capability is quite insignificant. The other phase is SBE, like in the electrodes, which is responsible for the ion mobility.

Remark 1. As to the homogenized composite constituting either the SBE or the separator, their characteristics are principally the same; however, the stiffness is higher and the mobility lower for the separator. As a consequence, there is no need to conceptually distinguish between these and they occupy the (union) domain Ω_e. □

3. 3D electro-chemo-mechanical problem – individual domains, interfaces and boundaries

3.1. Preliminaries

The time-continuous strong format and modeling assumptions for the individual domains, interfaces and boundaries are presented in the (general) 3D-setting. The material response is assumed to be linear(ized) with respect to mechanical properties, while nonlinear effects are allowed in terms of the electro-chemical response. Moreover, self-weight and any piezoelectric effects are ignored, isothermal conditions are assumed (for simplicity), and stress-assisted convection in the porous SBE is ignored (cf. Carlstedt et al. (2022c)).[1] The presentation closely follows those given elsewhere in further detail (Carlstedt et al., 2020, 2022b,a). Compared with previous work the separator phase is added in terms of both the electrochemical and mechanical problem formulation.

As to the notation of (sub)domains and surfaces in Fig. 3, the beam occupies the domain $\Omega = \hat{\Omega} \times [0, L]$, where $\hat{\Omega}$ represents the (uniform) cross-section located at $\bar{x} \in [0, L]$. The entire boundary is $\partial\Omega = \Gamma_{\text{ext}} \cup (\hat{\Omega} \times \{0\}) \cup (\hat{\Omega} \times \{L\})$ with $\Gamma_{\text{ext}} = \hat{\Gamma}_{\text{ext}} \times [0, L]$. Here, Γ_{ext} denotes the external surface of the beam, whereas $\hat{\Omega} \times \{0\}$ and $\hat{\Omega} \times \{L\}$ denote the end surface located at $\bar{x} = 0$ and $\bar{x} = L$, respectively. We also use the notation $\partial\hat{\Omega} = \hat{\Gamma}$ for consistency of notation. For $\boldsymbol{x} \in \Omega$, we may thus introduce the split $\boldsymbol{x} = \hat{\boldsymbol{x}} + \bar{x}\boldsymbol{e}_3 := (\hat{\boldsymbol{x}}, \bar{x}) \in \hat{\Omega} \times [0, L]$.

The fibers (embedded in the SBE in the upper and lower electrode), the SBE/separator occupy the subdomains $\Omega_f = (\hat{\Omega}_f^+ \cup \hat{\Omega}_f^-) \times [0, L]$ and $\Omega_e = \hat{\Omega}_e \times [0, L]$, respectively. The interior boundaries, which are interphases between fibers and the surrounding SBE, are denoted $\Gamma_{\text{fe}} = \hat{\Gamma}_{\text{fe}} \times [0, L]$.

3.2. Fiber and SBE/separator domains

The governing balance equations are as follows in the fiber domain Ω_f (for $t > 0$):

$$-\boldsymbol{\sigma} \cdot \boldsymbol{\nabla} = \boldsymbol{0} \tag{1a}$$

$$\boldsymbol{i} \cdot \boldsymbol{\nabla} = 0 \tag{1b}$$

$$\rho \partial_t c_{\text{Li}} + \boldsymbol{j}_{\text{Li}} \cdot \boldsymbol{\nabla} = 0 \tag{1c}$$

and in the SBE/separator domain Ω_e (for $t > 0$)

$$-\boldsymbol{\sigma} \cdot \boldsymbol{\nabla} = \boldsymbol{0} \tag{2a}$$

$$-\rho^F F[c_{\text{Li}} - c_{\text{X}}] + \boldsymbol{d} \cdot \boldsymbol{\nabla} = 0 \tag{2b}$$

$$\rho^F \partial_t c_{\text{Li}} + \boldsymbol{j}_{\text{Li}} \cdot \boldsymbol{\nabla} = 0 \tag{2c}$$

$$\rho^F \partial_t c_{\text{X}} + \boldsymbol{j}_{\text{X}} \cdot \boldsymbol{\nabla} = 0 \tag{2d}$$

where $\boldsymbol{\sigma}$ is the equilibrium stress, $\boldsymbol{i}$ is the (electronic) current density, $\boldsymbol{d}$ is the electric flux density (commonly known as dielectric displacement), $\boldsymbol{j}_{\text{Li}}$ and $\boldsymbol{j}_{\text{X}}$ are the flux, whereas c_{Li} and c_{X} are the concentration of Li-ions and (negatively charged) X-ions, respectively. Further, ρ is the solid (=total) density of the fiber (in Ω_f), whereas ρ^F is the fluid density of the electrolyte in the SBE/separator (in Ω_e). Finally, F is Faraday's constant.

Remark 2. Equation (1b), which represents electron transport in the fibers, implicitly means that Gauss law is satisfied with zero free charge, i.e. $\boldsymbol{d} \cdot \boldsymbol{\nabla} = 0$. □

---

[1] The reasoning for neglecting the stress assisted convection in the SBE, is because only minor effects on the electro-chemical performance due to mechanical loads (in particular, loads primarily acting in the fiber direction) were observed in Carlstedt et al. (2022c) for similar material systems.
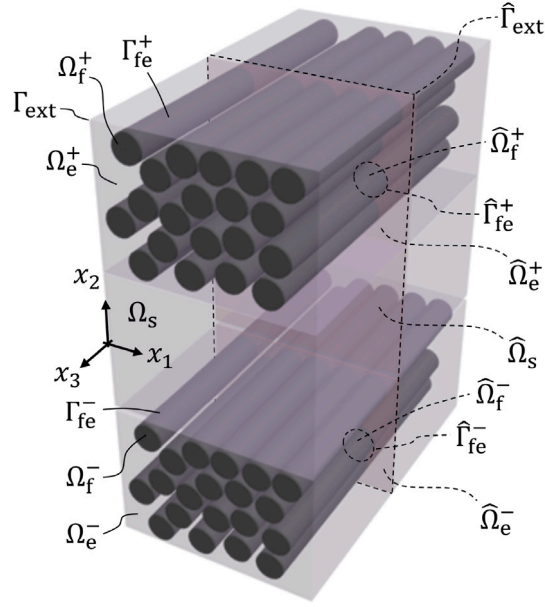
Fig. 3. Schematic illustration of beam segment in 3D with carbon fibers aligned with the beam axis. Pertinent notation.

The constitutive expressions, which are both of the energetic type (derivable from a free energy density, see Carlstedt et al. (2022b))[2] and of the dissipative type, are chosen as follows in the fiber domain Ω_f:

$$\boldsymbol{\sigma} = \mathbf{E} : \left[\boldsymbol{\epsilon}[\boldsymbol{u}] - \boldsymbol{\epsilon}^{\text{ch}}(c_{\text{Li}}) \right], \quad \boldsymbol{\epsilon}^{\text{ch}}(c_{\text{Li}}) = \boldsymbol{\alpha}^{\text{ch}} \left[c_{\text{Li}} - c_{\text{Li,ref}} \right] \tag{3a}$$

$$\boldsymbol{i} = -\kappa^{\text{f}} \boldsymbol{\nabla} \varphi \tag{3b}$$

$$\boldsymbol{j}_{\text{Li}} = -\boldsymbol{M}_{\text{Li}} \cdot \boldsymbol{\nabla} \mu_{\text{Li}} \tag{3c}$$

where the chemical potential μ_{Li} associated with Li is chosen as

$$\mu_{\text{Li}} = \mu_{\text{Li,ref}} + R\theta_{\text{ref}} \log \left(\frac{\gamma(c_{\text{Li}})\tilde{c}_{\text{Li}}}{\gamma(c_{\text{Li,ref}})\tilde{c}_{\text{Li,ref}}} \right) - \rho^{-1} \boldsymbol{\alpha}^{\text{ch}} : \boldsymbol{\sigma}(\boldsymbol{\epsilon}, c_{\text{Li}}) \tag{4}$$

The constitutive relation in (4) consists of two parts, representing: (i) standard concentration-driven diffusion and (ii) stress-driven diffusion (second part, i.e. $\rho^{-1} \boldsymbol{\alpha}^{\text{ch}} : \boldsymbol{\sigma}(\boldsymbol{\epsilon}, c_{\text{Li}})$), cf. Larché and Cahn (1973).

The corresponding constitutive expressions in the domain Ω_e are chosen as follows:

$$\boldsymbol{\sigma} = \mathbf{E} : \boldsymbol{\epsilon}[\boldsymbol{u}] \tag{5a}$$

$$\boldsymbol{d} = -\varepsilon \boldsymbol{\nabla} \varphi \tag{5b}$$

$$\boldsymbol{j}_{\text{Li}} = -\boldsymbol{M}_{\text{Li}} \cdot \boldsymbol{\nabla} \mu_{\text{Li}} - F \boldsymbol{M}_{\text{Li}} \cdot \boldsymbol{\nabla} \varphi \tag{5c}$$

$$\boldsymbol{j}_{\text{X}} = -\boldsymbol{M}_{\text{X}} \cdot \boldsymbol{\nabla} \mu_{\text{X}} + F \boldsymbol{M}_{\text{X}} \cdot \boldsymbol{\nabla} \varphi \tag{5d}$$

where the chemical potentials μ_{Li} and μ_{X} associated with Li and X, respectively, are obtained as

$$\mu_{\text{Li}} = \mu_{\text{Li,ref}} + R\theta_{\text{ref}} \log \left(\frac{\tilde{c}_{\text{Li}}}{\tilde{c}_{\text{Li,ref}}} \right) \tag{6a}$$

$$\mu_{\text{X}} = \mu_{\text{X,ref}} + R\theta_{\text{ref}} \log \left(\frac{\tilde{c}_{\text{X}}}{\tilde{c}_{\text{X,ref}}} \right) \tag{6b}$$

We introduced the following fields: $\boldsymbol{u}$ is the displacement and $\boldsymbol{\epsilon}[\boldsymbol{u}]$ is the corresponding (small) strain, φ is the electric potential. The normalized mass concentration of Li in the fibers is defined as $\tilde{c}_{\text{Li}} := \frac{c_{\text{Li}}}{c_{\text{Li,max}}}$ (with respect to the assumed maximum Li-concentration $c_{\text{Li,max}}$), while it is defined as $\tilde{c}_{\alpha} := \frac{c_{\alpha}}{c_{\alpha,\text{ref}}}$ (with respect to a reference concentration $c_{\alpha,\text{ref}}$) for $\alpha = \text{Li, X}$ (i.e., the Li$^+$ and X$^-$ ions in the SBE). We note that $c_{\text{Li,ref}}$ corresponds to an initial state, set as $c_{\text{Li,ref}}^{\text{f}} = 0.14$ in the fibers and $c_{\text{Li,ref}}^{\text{e}} = 1$

---

[2] The explicit expressions of the purely energetic quantities may be derived from introduced partial free energy densities (see in particular Appendix A of Carlstedt et al. (2022b) for more information).

in the SBE.[3] Further, $\gamma(c_{\mathrm{Li}})$ is a socalled activity function relevant to the fibers, for which a simple expression (adopted here) is $\gamma(c_{\mathrm{Li}}) = [1 - \tilde{c}_{\mathrm{Li}}]^{-1}$. Since Li is neutrally charged in the fibers, migration occurs only in Ω_{e}, whereas diffusion takes place in all phases.

The following material parameters are identified: $\mathbf{E}$ is the elasticity tensor,[4] ϵ^{ch} is the intercalation induced (free) strain characterized by the intercalation coefficient $\boldsymbol{\alpha}^{\mathrm{ch}}$,[5] κ^{f} is the electric (electronic) conductivity in the fibers, and $\varepsilon = \varepsilon_0 \varepsilon_r$ is the permittivity.[6] Further, $\boldsymbol{M}_{\mathrm{Li}}$ and $\boldsymbol{M}_{\mathrm{X}}$ are mobility tensors. Finally, R is the universal gas constant, whereas $c_{\mathrm{Li,ref}}$, $c_{\mathrm{X,ref}}$, $\mu_{\mathrm{Li,ref}}$, $\mu_{\mathrm{X,ref}}$, and θ_{ref} are reference values. It is noted that value $c_{\mathrm{Li,ref}}$ denotes the state at which no chemical strain is present in the material. Further, it may be noted that the initial values $\boldsymbol{\sigma} = \mathbf{0}$ and $\mu_{\mathrm{Li}} = \mu_{\mathrm{Li,ref}}$, $\mu_{\mathrm{X}} = \mu_{\mathrm{X,ref}}$, are obtained by setting $\epsilon = \mathbf{0}$ and $c_{\mathrm{Li}} = c_{\mathrm{Li,ref}}$, $c_{\mathrm{X}} = c_{\mathrm{X,ref}}$.

All constitutive tensors ($\boldsymbol{\alpha}^{\mathrm{ch}}$, $\mathbf{E}$, $\boldsymbol{M}_{\mathrm{Li}}$, $\boldsymbol{M}_{\mathrm{X}}$) represent assumed transverse isotropy in the fibers, whereas they represent isotropic response in the SBE/separator. Further, κ^{f} represents complete isotropy (as a reasonable model simplification since, as will be elaborated later, it is only the longitudinal conductivity that is of any relevance).

Next, using Faraday's law of electrolysis (while exploiting (5b)), we derive the constitutive relation for the current density:

$$\boldsymbol{i} = F[\boldsymbol{j}_{\mathrm{Li}} - \boldsymbol{j}_{\mathrm{X}}] = -F\boldsymbol{M}_{\mathrm{Li}} \cdot \boldsymbol{\nabla}\mu_{\mathrm{Li}} + F\boldsymbol{M}_{\mathrm{X}} \cdot \boldsymbol{\nabla}\mu_{\mathrm{X}} - \boldsymbol{\mathcal{K}} \cdot \boldsymbol{\nabla}\varphi \quad \text{in } \Omega_{\mathrm{e}} \tag{7}$$

where we introduced the ionic conductivity $\boldsymbol{\mathcal{K}} := F^2[\boldsymbol{M}_{\mathrm{Li}} + \boldsymbol{M}_{\mathrm{X}}]$.

Finally, we remark that isotropy prevails in the cross-sectional planes for all phases (fibers, SBE and separator), whereas the longitudinal planes may be anisotropic in the fibers. We also note that the "free" strain $\epsilon^{\mathrm{ch}}(c_{\mathrm{Li}})$ due to intercalation of ions in the fibers reflects the transverse isotropy.

Remark 3. The assumption of electroneutrality, i.e. $F[c_{\mathrm{Li}} - c_{\mathrm{X}}] = 0$, is often used in the electro-chemistry literature on conventional Li-ion batteries, see e.g. Newman and Thomas-Alyea (2004). However, the current model framework does not require this (unnecessary) condition. □

3.3. Interior boundaries

We assume that the displacement field $\boldsymbol{u}$ is continuous across the internal boundary Γ_{fe} (i.e. perfectly bonded). Further, we assume that μ_{Li} and φ may be discontinuous across Γ_{fe}, whereas the ion flux $j_{\mathrm{Li},n} := \boldsymbol{j}_{\mathrm{Li}} \cdot \boldsymbol{n}$ is continuous across Γ_{fe} from the SBE to the fibers. These discontinuities are modeled via linear interface relations involving the "electric resistance" (which turns to have a model structure that is similar to a linearized Butler-Volmer relation), expressed in terms of interface mobility $\mathcal{M}_{\mathrm{fe}}$ such that

$$j_{\mathrm{Li},n} = -\mathcal{M}_{\mathrm{fe}}[\![\mu_{\mathrm{Li}}]\!] - F\mathcal{M}_{\mathrm{fe}}[\![\varphi]\!] \quad \text{on } \Gamma_{\mathrm{fe}} \tag{8}$$

In Eq. (8), we introduced the jump operator $[\![\bullet]\!](\boldsymbol{x}) := \bullet(\boldsymbol{x}^{\mathrm{f}}) - \bullet(\boldsymbol{x}^{\mathrm{e}})$ and $\boldsymbol{x}^{\mathrm{f}} := \lim_{\epsilon\downarrow 0}[\boldsymbol{x} + \epsilon\boldsymbol{n}]$, $\boldsymbol{x}^{\mathrm{e}} := \lim_{\epsilon\downarrow 0}[\boldsymbol{x} - \epsilon\boldsymbol{n}]$ for $\boldsymbol{x} \in \Gamma_{\mathrm{fe}}$. Moreover, $\varphi^{\mathrm{e}} := \varphi(\boldsymbol{x}^{\mathrm{e}})$ is evaluated in the electrolyte at the fiber-electrolyte interface. The current density flux $i_n := \boldsymbol{i} \cdot \boldsymbol{n}$ across the interface Γ_{fe} is defined as

$$i_n = F[j_{\mathrm{Li},n} - \underbrace{j_{\mathrm{X},n}}_{=0}] = -F\mathcal{M}_{\mathrm{fe}}[\![\mu_{\mathrm{Li}}]\!] - \mathcal{K}_{\mathrm{fe}}[\![\varphi]\!] \quad \text{on } \Gamma_{\mathrm{fe}} \tag{9}$$

where we introduced the interface ionic conductivity $\mathcal{K}_{\mathrm{fe}} := F^2\mathcal{M}_{\mathrm{fe}}$. We note that the transport of X^- is blocked at the fiber-electrolyte interface. Further, we introduce the constitutive assumption for $d_n(= d_n^{\mathrm{f}}) := \boldsymbol{d} \cdot \boldsymbol{n}$ in terms of an interface permittivity $\mathcal{E}_{\mathrm{fe}}$:

$$d_n = -\mathcal{E}_{\mathrm{fe}}[\![\varphi]\!] \quad \text{on } \Gamma_{\mathrm{fe}} \tag{10}$$

At the SBE/separator interface we assume that the displacement field $\boldsymbol{u}$ and ion flux $j_{\alpha,n}$ (and electric current i_n) are continuous.

3.4. Exterior boundaries

With respect to the mechanical conditions, related to displacements ($\boldsymbol{u}$) and tractions ($\boldsymbol{t} := \boldsymbol{\sigma} \cdot \boldsymbol{n}$), we may, typically, choose the boundary conditions[7] for $t > 0$:

$$\begin{aligned}
&\bar{x} = 0: && \int_{\hat{\Omega}} u_1 \, \mathrm{d}\hat{\Omega} = \int_{\hat{\Omega}} u_2 \, \mathrm{d}\hat{\Omega} = 0, \ \int_{\hat{\Omega}} \left[u_1 x_2 - u_2 x_1\right] \mathrm{d}\hat{\Omega} = 0, \ u_3 = 0 \text{ on } \hat{\Omega} \times \{0\} \\
&\bar{x} = L: && \boldsymbol{t} = \mathbf{0} \text{ on } \hat{\Omega} \times \{L\} \\
&0 < \bar{x} < L: && \boldsymbol{t} = \boldsymbol{t}^{\mathrm{p}} \text{ on } \Gamma_{\mathrm{ext}}
\end{aligned} \tag{11}$$

---

[3] $c_{\mathrm{Li,ref}}$ in the fibers is defined as a non-zero value representing delithiated fibers (i.e. low ion concentration) while in the SBE it is set as 1 mol kg^{-1} (which corresponds to the assumed initial salt concentration in the electrolyte). The latter value is obtained from setting $\rho^{\mathrm{F}} c_{\mathrm{Li,max}} = 1$ molar (or 10^3 mol m^{-3}) and $\rho^{\mathrm{F}} = 10^3$ kg m^{-3}.

[4] More generally, $\mathbf{E}$ may depend on c_{Li} in the fibers; however, in this paper such dependence is ignored for the sake of simplicity.

[5] Intercalation strains in Ω_{e} is ignored.

[6] Piezoelectric effects are disregarded (as is commonly done in the electro-chemical literature).

[7] The chosen condition at the right end surface represents a free end, i.e. the actuator mode.

In (11), t^p refers to the prescribed traction acting on the external surfaces Γ_{ext}. For conditions related to ion flux ($j_{\text{Li},n} = \boldsymbol{j}_{\text{Li}} \cdot \boldsymbol{n}$, $j_{\text{X},n} = \boldsymbol{j}_{\text{X}} \cdot \boldsymbol{n}$), we choose for $t > 0$:

$$\begin{aligned}
\bar{x} = 0, L: \quad & j_{\text{Li},n} = 0 \text{ on } \hat{\Omega} \times \{0, L\} \\
& j_{X,n} = 0 \text{ on } \hat{\Omega}_{\text{e}} \times \{0, L\} \\
0 < \bar{x} < L: \quad & j_{\text{Li},n} = j_{X,n} = 0 \text{ on } \Gamma_{\text{ext}}
\end{aligned} \tag{12}$$

Further, for the electrical condition, related to the electric flux density (d_n), we set for $t > 0$:

$$\begin{aligned}
\bar{x} = 0, L: \quad & d_n = 0 \text{ on } \hat{\Omega}_{\text{e}} \times \{0, L\} \\
0 < \bar{x} < L: \quad & d_n = 0 \text{ on } \Gamma_{\text{ext}}
\end{aligned} \tag{13}$$

Finally, for the electric potential and current in the fibers, we set for $t > 0$:

$$\begin{aligned}
\bar{x} = 0: \quad & i_n = i_n^p \text{ on } \hat{\Omega}_{\text{f}}^+ \times \{0\}, \quad \varphi = 0 \text{ on } \hat{\Omega}_{\text{f}}^- \times \{0\} \\
\bar{x} = L: \quad & i_n = 0 \text{ on } \hat{\Omega}_{\text{f}}^+ \times \{L\}, \quad i_n = 0 \text{ on } \hat{\Omega}_{\text{f}}^- \times \{L\}
\end{aligned} \tag{14}$$

where i_n^p is the prescribed current.

4. Splitting the 3D-problem into axial beam (1D) and cross-sectional (2D) problems

4.1. Variationally consistent "two-scale" modeling — preliminaries

Our aim is to split the balance equations into two types of problems: (i) "beam" problems for $\bar{x} \in [0, L]$ and (ii) cross-sectional problems that are restricted to the cross-sectional planes $\hat{\Omega} \times \{\bar{x}\}$ for any given $\bar{x} \in [0, L]$. This "two-scale" format (of nested problems) is achieved via a variationally consistent split, cf. two-scale modeling involving homogenization. For a typical field z defined in $\hat{\Omega} \times [0, L]$, we then propose the ansatz[8]:

$$z(\hat{\boldsymbol{x}}, \bar{x}, t) = \bar{z}(\bar{x}, t) + \hat{z}(\hat{\boldsymbol{x}}, \bar{x}, t), \quad (\hat{z})' = 0 \quad (\hat{\boldsymbol{x}}, \bar{x}) \in \hat{\Omega} \times [0, L] \tag{15}$$

We note the complementary condition $(\hat{z})' = 0$. Now, for the SBE/separator domain, we shall (in this paper) always assume that $\bar{z} = 0$, i.e. the fields "localized" *a priori* to the cross-sectional planes.

The various balance problems will be considered in some detail subsequently.

4.2. Mechanical problem

In accordance with standard beam theory for small strain kinematics, we propose the following approximations (restrictions) of the displacement $\boldsymbol{u}$:

$$\begin{aligned}
\boldsymbol{u}(\hat{\boldsymbol{x}}, \bar{x}, t) = & \left[\bar{w}_1(\bar{x}, t) - \bar{\phi}(\bar{x}, t) x_2 \right] \boldsymbol{e}_1 + \left[\bar{w}_2(\bar{x}, t) + \bar{\phi}(\bar{x}, t) x_1 \right] \boldsymbol{e}_2 \\
& + \left[\bar{u}(\bar{x}, t) - \bar{w}_1'(\bar{x}, t) x_1 - \bar{w}_2'(\bar{x}, t) x_2 \right] \boldsymbol{e}_3 \\
& + \hat{\boldsymbol{u}}(\hat{\boldsymbol{x}}, \bar{x}, t)
\end{aligned} \tag{16}$$

which is complemented with the auxiliary conditions that ensure a unique split in (16):

$$\int_{\hat{\Omega}} \hat{\boldsymbol{u}} \, d\hat{\Omega} = \int_{\hat{\Omega}} \hat{\boldsymbol{x}} \times \hat{\boldsymbol{u}} \, d\hat{\Omega} = \boldsymbol{0}, \ \bar{x} \in (0, L) \tag{17}$$

where the part that represents cross-sectional deformations is denoted $\hat{\boldsymbol{u}} = \hat{u}_1 \boldsymbol{e}_1 + \hat{u}_2 \boldsymbol{e}_2$.[9] Here, $\bar{w}_\alpha$ are deflections of the midplane, $\bar{u}$ is the in-plane displacement in the midplane, whereas $\bar{\phi} = \bar{\phi}_3$ is the rotation of the cross-section. We also assume that $(\hat{\boldsymbol{u}})' = \boldsymbol{0}$ for $(\hat{\boldsymbol{x}}, \bar{x}) \in \hat{\Omega} \times [0, L]$, whereby it follows that the strain becomes

$$\begin{aligned}
\boldsymbol{\epsilon} = [\boldsymbol{u} \otimes \nabla]^{\text{sym}} = & -\bar{\phi}' x_2 \left[\boldsymbol{e}_1 \otimes \boldsymbol{e}_3 \right]^{\text{sym}} + \bar{\phi}' x_1 \left[\boldsymbol{e}_2 \otimes \boldsymbol{e}_3 \right]^{\text{sym}} \\
& + \left[\bar{u}' - \bar{w}_1'' x_1 - \bar{w}_2'' x_2 \right] \boldsymbol{e}_3 \otimes \boldsymbol{e}_3 + \hat{\boldsymbol{\epsilon}}
\end{aligned} \tag{18}$$

where $\hat{\boldsymbol{\epsilon}} = \hat{\epsilon}_{\alpha\beta} \boldsymbol{e}_\alpha \otimes \boldsymbol{e}_\beta = [\hat{\boldsymbol{u}} \otimes \nabla]^{\text{sym}} = \hat{\boldsymbol{I}} \cdot \boldsymbol{\epsilon}[\boldsymbol{u}] \cdot \hat{\boldsymbol{I}}$ is the strain in the cross-sectional plane(s) $\hat{\Omega} \times \{\bar{x}\}$ for $\bar{x} \in (0, L)$.

Henceforth, we restrict to the situation of plane bending (for the sake of simplicity), defined by $\bar{w}_1 = \bar{\phi} = 0$, $\bar{w}_2 := \bar{w}$, whereby we obtain

$$\boldsymbol{\epsilon} = \left[\bar{\epsilon} + \bar{\kappa} x_2 \right] \boldsymbol{e}_3 \otimes \boldsymbol{e}_3 + \hat{\boldsymbol{\epsilon}} \tag{19}$$

with $\bar{\epsilon} := \bar{u}'$, $\bar{\kappa} := -\bar{w}''$ denoting the axial strain in the midplane and the curvature, respectively. Finally, we introduce the approximation $\hat{\boldsymbol{u}}' = \boldsymbol{0}$, whereby we obtain $\epsilon_{13} = \epsilon_{23} = 0$ (which is the standard condition in the Euler–Bernoulli beam theory[10]).

---

[8] The simplified notation is used: $\{\bullet\}' := \frac{\partial \{\bullet\}}{\partial \bar{x}}$.

[9] Note that $\hat{\boldsymbol{u}} \neq \hat{\boldsymbol{I}} \cdot \boldsymbol{u}$.

[10] It is a trivial fact that σ_{13} and σ_{23} are generally non-zero in order to maintain equilibrium.

We may now show (from the weak format, based on the specific kinematic assumptions introduced above) that the equilibrium Eqs. (1a) and (2a), which are valid in 3D, can be split into equilibrium equations of two different types:

(i) Beam problem:

$$-\left[\bar{M}' + \bar{r}\right]' = \bar{q} \quad \text{in } [0, L], t > 0 \tag{20a}$$

$$-\bar{N}' = \bar{f} \quad \text{in } [0, L], t > 0 \tag{20b}$$

where the bending moment $\bar{M}(\bar{x}, t)$, the normal force $\bar{N}(\bar{x}, t)$, and the loadings $\bar{q}(\bar{x}, t)$, $\bar{r}(\bar{x}, t)$, $\bar{f}(\bar{x}, t)$ can be expressed as

$$\bar{M} := \int_{\hat{\Omega}} \sigma_{33} x_2 \, d\hat{\Omega}, \quad \bar{N} := \int_{\hat{\Omega}} \sigma_{33} \, d\hat{\Omega}, \quad \bar{q} := \int_{\hat{\Gamma}} t_2^{\mathrm{p}} \, d\hat{\Gamma}, \quad \bar{r} := \int_{\hat{\Gamma}} t_3^{\mathrm{p}} x_2 \, d\hat{\Gamma}, \quad \bar{f} := \int_{\hat{\Gamma}} t_3^{\mathrm{p}} \, d\hat{\Gamma} \tag{21}$$

The (quite trivial) expression for σ_{33}, by which $\bar{M}$ and $\bar{N}$ can be calculated, is given for completeness: Using the kinematic assumption (15), we obtain

$$\sigma_{33}(\hat{u}, \bar{\epsilon}, \bar{\kappa}, c_{\mathrm{Li}}) = \hat{E} : \hat{\epsilon} + (\mathbf{E})_{3333} \left[\bar{\epsilon} + \bar{\kappa} x_2\right] + \sigma_{33}^{\mathrm{ch}}(c_{\mathrm{Li}}) \tag{22}$$

and

$$\sigma_{33}^{\mathrm{ch}}(c_{\mathrm{Li}}) = -\hat{E} : \hat{\epsilon}^{\mathrm{ch}}(c_{\mathrm{Li}}) - (\mathbf{E})_{3333} \epsilon_{33}^{\mathrm{ch}}(c_{\mathrm{Li}}) \tag{23}$$

where $(\hat{E})_{\alpha\beta} = (\mathbf{E})_{\alpha\beta 33} = (\mathbf{E})_{33\alpha\beta}$.[11] It is noted that $\hat{E}$ represents out-of-plane anisotropy and $(\hat{E})_{12} = (\hat{E})_{21} = 0$. Further, the modulus $(\mathbf{E})_{3333}$ represents uniaxial strain (and not uniaxial stress as in the classical beam theory).

It is possible to derive variationally consistent boundary conditions. For example, the clamped left end is defined by the conditions.[12]

$$\bar{x} = 0 : \quad \bar{w} = 0, \ (\bar{w})' = 0, \ \bar{u} = 0 \tag{24}$$

(ii) Cross-sectional problem:

$$-\hat{\sigma} \cdot \hat{\nabla} = \mathbf{0} \quad \text{in } \hat{\Omega}, \ x_3 \in (0, L), t > 0 \tag{25}$$

where $\hat{\sigma} = \hat{I} \cdot \sigma \cdot \hat{I}$ is the stress in the cross-sectional plane $\hat{\Omega}$. The pertinent boundary conditions, which hold for each $\bar{x} \in (0, L)$, are:

$$\int_{\hat{\Omega}} \hat{u} \, d\hat{\Omega} = \int_{\hat{\Omega}} \hat{x} \times \hat{u} \, d\hat{\Omega} = \mathbf{0} \tag{26a}$$

$$\hat{t} = \hat{t}^{\mathrm{p}} \text{ on } \hat{\Gamma}_{\mathrm{ext}} \tag{26b}$$

4.3. Electric problem in fibers

We consider the balance Eq. (1b) for the current density in the fibers. The electric potential in the fibers is *assumed uniform* in the cross-sectional domains $\hat{\Omega}_{\mathrm{f}}^{+/-}$, whereas it may vary along the fibers; hence,

$$\varphi(\hat{x}, \bar{x}, t) = \bar{\varphi}^{+/-}(\bar{x}, t) \quad (\hat{x}, \bar{x}) \in \hat{\Omega}_{\mathrm{f}}^{+/-} \times [0, L] \tag{27}$$

i.e. $\hat{\varphi} = 0$, whereby the electric field becomes $e = \bar{e}^{+/-} e_3$ with $\bar{e}^{+/-} := -(\bar{\varphi}^{+/-})'$

We may now show (from the weak format, based on the specific assumption on the electric potential introduced above) that the balance Eq. (1b), which is valid in 3D, reduces to the beam problem (in 1D)

$$(\bar{I}^{+/-})' - \bar{s}^{+/-} = 0 \quad \text{in } [0, L], t > 0 \tag{28}$$

where

$$\bar{I}^{+/-} := \int_{\hat{\Omega}_{\mathrm{f}}^{+/-}} i_3 \, d\hat{\Omega}, \quad \bar{s}^{+/-} := -\int_{\hat{\Gamma}_{\mathrm{fe}}^{+/-}} i_n \, d\hat{\Gamma} \tag{29}$$

Here, we introduced $\bar{I}^{+/-}(\bar{x}, t)$ as the total current flux in the fibers (collectively) in the upper (+) and lower (-) electrodes, respectively, whereas $\bar{s}^{+/-}(\bar{x}, t)$ is the "current source", i.e. the current entering the fiber domain via Li-ion transport from the surrounding SBE. It is thus concluded that, from a hierarchical viewpoint, only a macroscale problem is at hand, whereas the subscale problems in the cross-sections are absent. Since $i_3 = -\kappa^{\mathrm{f}}(\bar{\varphi}^{+/-})'$, it follows that $\bar{I}^{+/-}$ has the following simple constitutive relation

$$\bar{I}^{+/-} = -\mathcal{K}^{\mathrm{f},+/-}(\bar{\varphi}^{+/-})' \quad \text{with } \mathcal{K}^{\mathrm{f},+/-} := |\hat{\Omega}_{\mathrm{f}}^{+/-}| \kappa^{\mathrm{f}} \tag{30}$$

---

[11] Latin indices range from 1 to 3, whereas Greek indices range from 1 to 2 and, thus, refer to restrictions to the cross-sectional plane.

[12] The homogeneous b.c. at the left end follow from the conditions in (11) on u_2, u_3 together with the split in (16) and condition (15). The condition on u_1 in (11) is automatically satisfied.
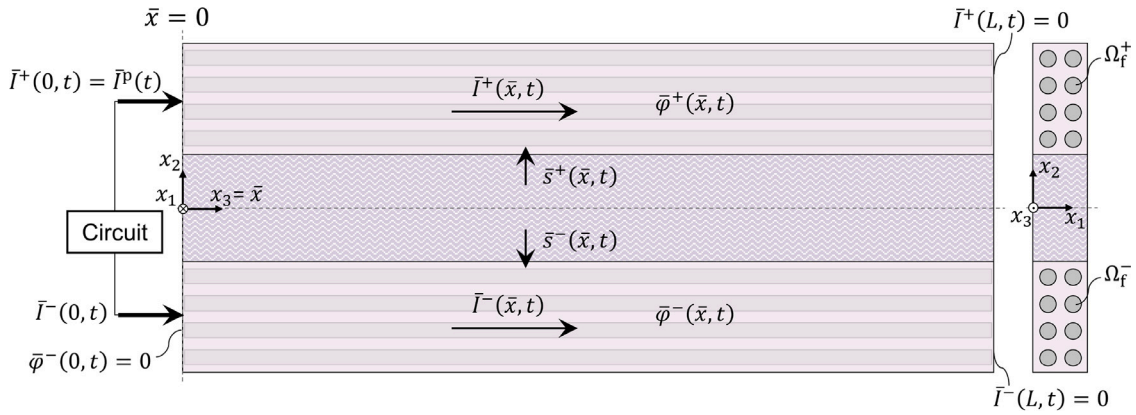
Fig. 4. Electrochemical variables in beam structure comprising two electrodes and a separator. (Mechanical boundary conditions are not shown; they differ between the sensor and actuator modes.).

Finally, the pertinent boundary conditions become

$$\begin{aligned}
\bar{x} = 0: \quad & \bar{I}^+ = \bar{I}^{\mathrm{p}}(t) := - \int_{\hat{\Omega}_{\mathrm{f}}^+ \times \{0\}} i_n^{\mathrm{p}} \, \mathrm{d}\hat{\Omega}, \quad & \bar{\varphi}^- = \bar{\varphi}^{\mathrm{p}}(t) \\
\bar{x} = L: \quad & \bar{I}^+ = 0, \quad & \bar{I}^- = 0
\end{aligned} \tag{31}$$

We note that the electric current is applied/extracted to/from the fiber electrodes at the fixed support ($\bar{x} = 0$), whereas the right end ($\bar{x} = L$) is assumed to be electrically insulated. As a consequence, it is possible to use experimental results (Johannisson et al., 2020; Harnden et al., 2022) for the verification and validation of the computationally predicted performance. Further, we set the prescribed potential at the negative fiber as $\bar{\varphi}^{\mathrm{p}}(t) = 0$.

4.4. Electro-chemical problem

We consider the balance Eq. (2b) for the electric charge in the SBE-separator. It is assumed the $\varphi = \hat{\varphi}$, i.e. $\bar{\varphi} = 0$, with the assumption $\varphi' = 0$ for $(\hat{x}, \bar{x}) \in \hat{\Omega}_{\mathrm{e}} \times [0, L]$, whereby the electric field becomes $e := -\nabla\varphi = -\hat{I} \cdot \nabla\varphi = -\hat{\nabla}\varphi$. The assumption that the electric field in the electrolyte along the beam is negligible, is motivated by the large difference between the electronic conductivity in the fibers and the ion conductivity of the SBE-separator phases.

We may now show (from the weak format) that the balance Eq. (2b), which is valid in 3D, reduces to the cross-sectional 2D-problem for any given $\bar{x} \in (0, L)$:

$$-\rho^{\mathrm{F}} F[c_{\mathrm{Li}} - c_{\mathrm{X}}] + \hat{d} \cdot \hat{\nabla} = 0 \text{ in } \hat{\Omega}_{\mathrm{e}}, t > 0 \tag{32a}$$

Clearly, in this case there is no macroscale problem present.

Finally, we consider the balance Eq. (1c) and (2c), (2d) for the ionic transport in the fibers as well as in the SBE-separator. Like for the electric potential, we assume that $\mu_{\mathrm{Li}} = \hat{\mu}_{\mathrm{Li}}$, $\mu_{\mathrm{X}} = \hat{\mu}_{\mathrm{X}}$, with the assumption $(\mu_{\mathrm{Li}})' = (\mu_{\mathrm{X}})' = 0$, whereby $\nabla\mu_{\mathrm{Li}} = \hat{I} \cdot \nabla\mu_{\mathrm{Li}} = \hat{\nabla}\mu_{\mathrm{Li}}$ and $\nabla\mu_{\mathrm{X}} = \hat{I} \cdot \nabla\mu_{\mathrm{X}} = \hat{\nabla}\mu_{\mathrm{X}}$.

We may now show (from the weak format) that the pertinent balance equations reduce to 2D problems for any given $\bar{x} \in (0, L)$:

$$\rho \partial_t c_{\mathrm{Li}} + \hat{j}_{\mathrm{Li}} \cdot \hat{\nabla} = 0 \text{ in } \hat{\Omega}_{\mathrm{f}}, t > 0 \tag{33a}$$

$$\rho^{\mathrm{F}} \partial_t c_\alpha + \hat{j}_\alpha \cdot \hat{\nabla} = 0 \text{ in } \hat{\Omega}_{\mathrm{e}}, t > 0 \tag{33b}$$

where (33a) and (33b) represent the mass balance of Li$^+$ in the fibers, and Li$^+$ and X$^-$ in the electrolyte phase, respectively. Even in this case the macroscale problem is absent.

5. "Two-scale" problem for sensor and actuator modes

5.1. Preliminaries

Consider the beam segment with the sketchy cross-section in Fig. 4. Once again, we note that the separator layer is waferred between two identical electrode layers. Without obscuring generality, we assume henceforth that the surface load is absent, i.e. $t^{\mathrm{p}} = 0$, such that $q = r = f = 0$ in (20a) and (20b). Further, since $\hat{t}^{\mathrm{p}} = 0$ on $\hat{\Gamma}_{\mathrm{ext}}$ for any $\bar{x} \in [0, L]$, the cross-sections are not subjected to any external loading.

5.2. General setting — fibers with finite conductivity

For suitably chosen function spaces $\bar{\mathbb{F}}^+, \bar{\mathbb{F}}^-, \bar{\mathbb{U}}, \bar{\mathbb{W}}$, containing the Dirichlet boundary conditions e.g. defined in Eqs. (24) and (31), we pose the "structural" (beam) problem: For a given time $t = t_n$, find $\bar{\varphi}^+(\bullet, t_n) \in \bar{\mathbb{F}}^+$, $\bar{\varphi}^-(\bullet, t_n) \in \bar{\mathbb{F}}^-$, $\bar{u}(\bullet, t_n) \in \bar{\mathbb{U}}$, $\bar{w}(\bullet, t_n) \in \bar{\mathbb{W}}$, that solve

$$\int_0^L (\delta\bar{\varphi})' \bar{I}^+(\bar{e}^+) \,dx - \int_0^L \delta\bar{\varphi}\, \bar{s}^+\{\bar{\kappa}, \bar{\epsilon}, \bar{\varphi}^+, \bar{\varphi}^-\} \,dx = \delta\bar{\varphi}(0)\bar{I}^{\mathrm{p}}(t_n), \qquad \forall \delta\bar{\varphi} \in \bar{\mathbb{F}}^{+,0} \tag{34a}$$

$$\int_0^L (\delta\bar{\varphi})' \bar{I}^-(\bar{e}^-) \,dx - \int_0^L \delta\bar{\varphi}\, \bar{s}^-\{\bar{\kappa}, \bar{\epsilon}, \bar{\varphi}^+, \bar{\varphi}^-\} \,dx = 0, \qquad \forall \delta\bar{\varphi} \in \bar{\mathbb{F}}^{-,0} \tag{34b}$$

$$\int_0^L (\delta\bar{u})' \bar{N}\{\bar{\kappa}, \bar{\epsilon}, \bar{\varphi}^+, \bar{\varphi}^-\} \,dx = 0, \qquad \forall \delta\bar{u} \in \bar{\mathbb{U}}^0 \tag{34c}$$

$$\int_0^L (\delta\bar{w})'' \bar{M}\{\bar{\kappa}, \bar{\epsilon}, \bar{\varphi}^+, \bar{\varphi}^-\} \,dx = 0, \qquad \forall \delta\bar{w} \in \bar{\mathbb{W}}^0 \tag{34d}$$

where $\bar{\mathbb{F}}^{-,0}, \bar{\mathbb{F}}^{+,0} \bar{\mathbb{U}}^0, \bar{\mathbb{W}}^0$ are test spaces with homogeneous boundary values corresponding to the Dirichlet boundary conditions.

To close the problem, it is necessary to find constitutive relations for $\bar{s}^{+/-}, \bar{N}, \bar{M}$ in terms of the "structural" fields $\bar{\varphi}^+(\bullet, t_n)$, $\bar{\varphi}^-(\bullet, t_n)$, $\bar{w}(\bullet, t_n)$, $\bar{u}(\bullet, t_n)$. More precisely, the problem (34) is solved in a nested fashion with the cross-sectional problem subjected to *potentiostatic* control for any given position $\bar{x} \in (0, L)$ and t_n (pertinent to a given time-step): Given values $\bar{\kappa} := -\bar{w}''$, $\bar{\epsilon} := \bar{u}', \bar{\varphi}^+, \bar{\varphi}^-$, the cross-sectional problem is solved for the local fields[13] $Z := (\hat{u}, \varphi, c_{\mathrm{Li}}, c_{\mathrm{X}}, \mu_{\mathrm{Li}}, \mu_{\mathrm{X}}) = Z\{\bar{\kappa}, \bar{\epsilon}, \bar{\varphi}^+, \bar{\varphi}^-\}$, by which we are able to compute values of $\bar{s}^{+/-}(Z\{\bar{\kappa}, \bar{\epsilon}, \bar{\varphi}^+, \bar{\varphi}^-\}) = \bar{s}^{+/-}\{\bar{\kappa}, \bar{\epsilon}, \bar{\varphi}^+, \bar{\varphi}^-\}$, $\bar{M}(\bar{\kappa}, \bar{\epsilon}; Z\{\bar{\kappa}, \bar{\epsilon}, \bar{\varphi}^+, \bar{\varphi}^-\}) = \bar{M}\{\bar{\kappa}, \bar{\epsilon}, \bar{\varphi}^+, \bar{\varphi}^-\}$, and $\bar{N}(\bar{\kappa}, \bar{\epsilon}; Z\{\bar{\kappa}, \bar{\epsilon}, \bar{\varphi}^+, \bar{\varphi}^-\}) = \bar{N}\{\bar{\kappa}, \bar{\epsilon}, \bar{\varphi}^+, \bar{\varphi}^-\}$. Clearly, in order to obtain these values we need to solve the fully coupled electro-chemo-mechanical problem in the considered time-step, involving all the active phases: Fibers, SBE and separator. The relevant weak form is shown in the next Subsection.

5.3. Electro-chemo-mechanical problem pertinent to the beam cross-section

The weak format for the potentiostatic problem will be established for the time-integrated problem: For given "macroscale" values $\bar{\kappa}, \bar{\epsilon}, \bar{\varphi}^+, \bar{\varphi}^-$ at location $\bar{x}$ and time t_n: Find the fields $\hat{u}$, φ, μ_{Li}, μ_{X}, c_{Li}, c_{X} in the appropriate function spaces (with the appropriate regularity and satisfying essential boundary conditions) together with the Lagrange multipliers that solve

$$\int_{\hat{\Omega}} \hat{\boldsymbol{\sigma}} : \hat{\epsilon}[\delta\hat{\boldsymbol{u}}] \,d\hat{\Omega} + \bar{\lambda}_{\mathrm{T}} \cdot \int_{\hat{\Omega}} \delta\hat{\boldsymbol{u}} \,d\hat{\Omega} + \bar{\lambda}_{\mathrm{R}} \cdot \int_{\hat{\Omega}} \hat{\boldsymbol{x}} \times \delta\hat{\boldsymbol{u}} \,d\hat{\Omega} = 0 \tag{35a}$$

$$\int_{\hat{\Omega}_{\mathrm{e}}} \rho^{\mathrm{F}} F \left[c_{\mathrm{Li}} - c_{\mathrm{X}} \right] \delta\varphi \,d\hat{\Omega} + \int_{\hat{\Omega}_{\mathrm{e}}} \hat{\boldsymbol{d}} \cdot \hat{\boldsymbol{\nabla}}[\delta\varphi] \,d\hat{\Omega} - \int_{\hat{\Gamma}_{\mathrm{fe}}} \hat{d}_n \,[\![\delta\varphi]\!] \,d\hat{\Gamma} = 0 \tag{35b}$$

$$-\frac{1}{\Delta t} \left[\int_{\hat{\Omega}_{\mathrm{f}}} \rho \left[c_{\mathrm{Li}} - {}^{n-1}c_{\mathrm{Li}} \right] \delta\mu_{\mathrm{Li}} \,d\hat{\Omega} + \int_{\hat{\Omega}_{\mathrm{e}}} \rho^{\mathrm{F}} \left[c_{\mathrm{Li}} - {}^{n-1}c_{\mathrm{Li}} \right] \delta\mu_{\mathrm{Li}} \,d\hat{\Omega} \right]$$

$$+ \int_{\hat{\Omega}} \hat{\boldsymbol{j}}_{\mathrm{Li}} \cdot \hat{\boldsymbol{\nabla}}[\delta\mu_{\mathrm{Li}}] \,d\hat{\Omega} + \int_{\hat{\Gamma}_{\mathrm{fe}}} \hat{j}_{\mathrm{Li},n} \,[\![\delta\mu_{\mathrm{Li}}]\!] \,d\hat{\Gamma} = 0 \tag{35c}$$

$$-\frac{1}{\Delta t} \int_{\hat{\Omega}_{\mathrm{e}}} \rho^{\mathrm{F}} \left[c_{\mathrm{X}} - {}^{n-1}c_{\mathrm{X}} \right] \delta\mu_{\mathrm{X}} \,d\hat{\Omega} + \int_{\hat{\Omega}_{\mathrm{e}}} \hat{\boldsymbol{j}}_{\mathrm{X}} \cdot \hat{\boldsymbol{\nabla}}[\delta\mu_{\mathrm{X}}] \,d\hat{\Omega} = 0 \tag{35d}$$

$$\int_{\hat{\Omega}} \left[\mu_{\mathrm{Li}}^{\mathrm{en}} - \mu_{\mathrm{Li}} \right] \delta c_{\mathrm{Li}} \,d\hat{\Omega} = 0 \tag{35e}$$

$$\int_{\hat{\Omega}_{\mathrm{e}}} \left[\mu_{\mathrm{X}}^{\mathrm{en}} - \mu_{\mathrm{X}} \right] \delta c_{\mathrm{X}} \,d\hat{\Omega} = 0 \tag{35f}$$

$$\delta\bar{\lambda}_{\mathrm{T}} \cdot \int_{\hat{\Omega}} \hat{\boldsymbol{u}} \,d\hat{\Omega} = 0 \tag{35g}$$

$$\delta\bar{\lambda}_{\mathrm{R}} \cdot \int_{\hat{\Omega}} \hat{\boldsymbol{x}} \times \hat{\boldsymbol{u}} \,d\hat{\Omega} = 0 \tag{35h}$$

for suitably chosen test functions $\delta\hat{\boldsymbol{u}}$, etc. It appears that $\bar{\lambda}_{\mathrm{T}} = \boldsymbol{0}$ and $\bar{\lambda}_{\mathrm{R}} = \bar{\lambda}_{\mathrm{R}} \boldsymbol{e}_3 = \boldsymbol{0}$.

5.4. Extreme situation — perfectly conducting fibers

We may assume that the *fibers are perfect electronic conductors*, i.e. $\mathcal{K}^{\mathrm{f},+/-} \to \infty$, whereby we conclude that $\bar{\varphi}^+$ and $\bar{\varphi}^-$ do not depend on $\bar{x}$, i.e.

$$\bar{\varphi}^+(\bar{x}, t) = \bar{\Phi}^+(t), \quad \bar{\varphi}^-(\bar{x}, t) = \bar{\Phi}^-(t) = 0 \tag{36}$$

---

[13] Clearly these values also depend on c_α from the previous time step. This dependency is omitted for brevity.

whereby it is noted that only $\bar{\Phi}^+(t)$ is part of the solution. The boundary condition $\bar{I}^+(0,t) = \bar{I}^p(t)$ still holds. As a consequence, we have the simplified functional expressions $\bar{s}^+(Z\{\bar{\kappa},\bar{\epsilon},\bar{\Phi}^+,0\}) = \bar{s}^+\{\bar{\kappa},\bar{\epsilon},\bar{\Phi}^+,0\}$, $\bar{M}(\bar{\kappa},\bar{\epsilon};Z\{\bar{\kappa},\bar{\epsilon},\bar{\Phi}^+,0\}) = \bar{M}\{\bar{\kappa},\bar{\epsilon},\bar{\Phi}^+,0\}$, and $\bar{N}(\bar{\kappa},\bar{\epsilon};Z\{\bar{\kappa},\bar{\epsilon},\bar{\Phi}^+,0\}) = \bar{N}\{\bar{\kappa},\bar{\epsilon},\bar{\Phi}^+,0\}$. This situation will be considered exclusively henceforth in this paper.

Special case: Sensor mode

Used as a sensor, the beam is loaded by the prescribed end displacement $\bar{w}(L,t) = \bar{w}^p(t)$. The problem thus becomes: Solve for $\bar{\Phi}^+(t_n) \in \mathbb{R}$ and the fields $\bar{u}(\bullet,t_n) \in \bar{\mathbb{U}}, \bar{w}(\bullet,t_n) \in \bar{\mathbb{W}}$ from

$$-\int_0^L \bar{s}^+\{\bar{\kappa},\bar{\epsilon},\bar{\Phi}^+,0\}\,\mathrm{d}x = \bar{I}^p(t), \tag{37a}$$

$$\int_0^L (\delta\bar{u})' \bar{N}\{\bar{\kappa},\bar{\epsilon},\bar{\Phi}^+,0\}\,\mathrm{d}x = 0, \qquad\qquad \forall \delta\bar{u} \in \bar{\mathbb{U}}^0 \tag{37b}$$

$$\int_0^L (\delta\bar{w})'' \bar{M}\{\bar{\kappa},\bar{\epsilon},\bar{\Phi}^+,0\}\,\mathrm{d}x = 0, \qquad\qquad \forall \delta\bar{w} \in \bar{\mathbb{W}}^0 \tag{37c}$$

Remark 4. The primary output quantity is $\bar{\Phi}^+(t)$, which is part of the solution. □

Special case: Actuator mode

Used as an actuator, the beam is externally unloaded and deforms freely when subjected to "electrochemical loading" only. Now, since it is assumed that the solution $\bar{\Phi}^+(t)$ is independent on $\bar{x}$, we conclude that $\bar{\kappa}$ and $\bar{\epsilon}$ must also be independent on $\bar{x}$, and we may set $\bar{\kappa}(\bar{x},t) := \bar{K}(t)$ and $\bar{\epsilon}(\bar{x},t) := \bar{E}(t)$. In other words, each beam cross-section is completely equivalent and it is sufficient to solve the electro-chemo-mechanical problem only once. As a result, the structural problem simplifies to that of finding $\bar{K}(t_n) \in \mathbb{R}, \bar{E}(t_n) \in \mathbb{R}, \bar{\Phi}^+(t_n) \in \mathbb{R}$ that solve

$$\bar{s}^+\{\bar{K},\bar{E},\bar{\Phi}^+,0\} = -\bar{s}^p(t_n), \tag{38a}$$

$$\bar{N}\{\bar{K},\bar{E},\bar{\Phi}^+,0\} = 0. \tag{38b}$$

$$\bar{M}\{\bar{K},\bar{E},\bar{\Phi}^+,0\} = 0. \tag{38c}$$

where $\bar{s}^p(t_n) = \frac{\bar{I}^p(t_n)}{L}$. In practice this means that the corresponding cross-section problem can be solved under galvanostatic control with prescribed $\bar{s}^+ = \bar{s}^p(t_n)$ and $\bar{\Phi}^-(t_n) = 0$.

Remark 5. Reconsider the balance equation in the strong format for the upper electrode:

$$(\bar{I}^+)' - \bar{s}^p(t) = 0, \quad \bar{x} \in (0,L), t > 0 \tag{39}$$

which has the simple solution

$$\bar{I}^+(\bar{x},t) = \bar{I}^p(t)\left[1 - \frac{\bar{x}}{L}\right], \quad \bar{x} \in (0,L), t > 0 \tag{40}$$

where we used the boundary condition $\bar{I}^+(L,t) = 0$. This solution clearly satisfies $\bar{I}^+(0,t) = \bar{I}^p(t)$. □

Finally, when $\bar{K}(t)$ has been computed it is trivial to compute the beam deflection $\bar{w}(\bar{x},t) = -\frac{1}{2}\bar{K}(t)[\bar{x}]^2$. The end deflection is $\bar{w}(L,t) = -\frac{1}{2}\bar{K}(t)L^2$.

6. Results and discussion

6.1. Problem description — preliminaries

The geometry and chosen FE-mesh are illustrated in Figs. 5a-b. Dimensions, i.e. beam length (L), layers/laminae thickness (electrode: h_{ele}, separator: h_{sep}), widths (beam: w_{beam}, 2D-model: w_{ext}) and fiber volume fraction ($V_f = 0.43$), are chosen from Johannisson et al. (2020).

For the sensor mode, the finite element solution of the beam problem is obtained in an iterative manner using MATLAB, while the solution of the cross-sectional (2D) problem is obtained using the weak form PDE module in COMSOL Multiphysics version 5.4 (Fig. 5c). However, for the actuation and prelithiation (described in Section 6.2) problems, the cross-sectional problem is solved directly in COMSOL while the beam response is obtained from post-processing. The solution algorithm is described in Appendix A.

The used parameter values are listed in Table B.2 (in Appendix B). How these values are chosen is discussed at length in Carlstedt et al. (2020, 2022c,a). Here, we merely note the following: Elastic moduli (defining **E**) and ion mobilities (defining $\boldsymbol{\eta}$) for the porous SBE and separator phases are estimated from the Bruggeman relation (Doyle et al., 1993; Bruggeman, 1937) in terms of the porosity ($\phi^e = 0.4$ for the SBE and $\phi^{sep} = 0.5$ for the separator) and Bruggeman's constants (b^e and b^{sep}). Values of the chemical expansion coefficients (defining $\boldsymbol{\alpha}^{ch}$) for the fibers are taken from Johannisson et al. (2020), Jacques et al. (2013a). Further, we set $c_{Li,max} = C^f 3600/F$, where C^f is the assumed (maximum) specific capacity for carbon fibers measured at very low (dis)charge current, cf. Johannisson et al. (2020), Jacques et al. (2013a). Finally, the reference value $\mu_{Li,ref}$ for Li in the fibers is taken from Kjell et al. (2013), while we set $\mu_{Li,ref} = 0$ in the SBE and separator.
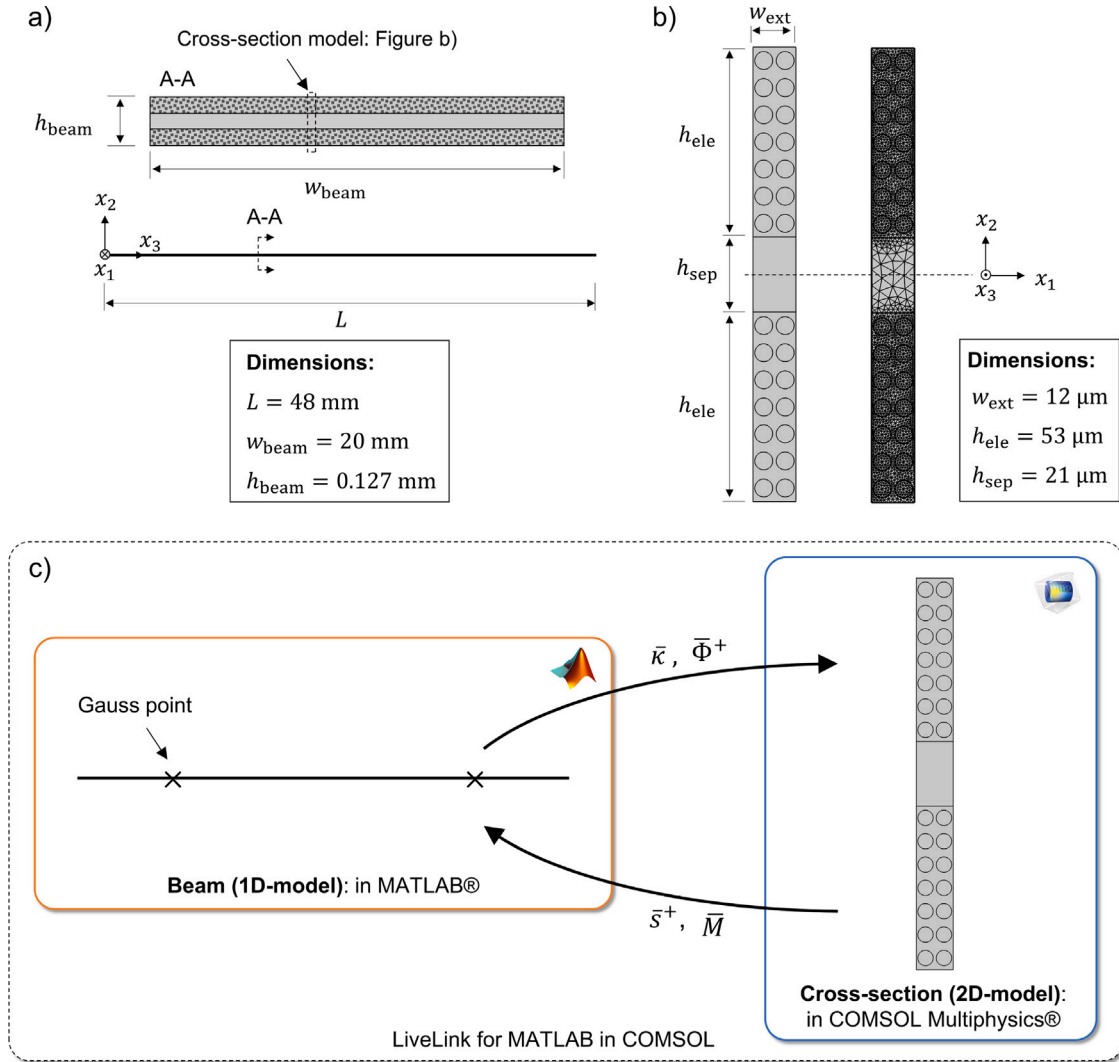
Fig. 5. Model geometries and FE-mesh for (a) the 1D beam model, modeled using one element with two Gauss points, and (b) the 2D cross-section model, modeled using triangular Lagrange elements. (c) Schematic illustration of model implementation done using the MATLAB-COMSOL LiveLink interface.

6.2. Prelithiation of fibers (activation step)

In accordance with the experimental procedure in Johannisson et al. (2020), Harnden et al. (2022), we first simulate the prelithiation (or activation) process of the two electrodes independently. The prelithiated state constitutes the initial condition for the sensor and actuator simulations. The process corresponds to simulation of two separate (negative) half-cells (Fig. 6a), one for each electrode, simultaneously (cf. Carlstedt et al. (2020)).

Fig. 6a shows $\bar{\Phi}^+(t)$ and $\bar{\Phi}^-(t)$ for the two half-cells during the lithiation process with current $\bar{I}^p = 5.9 \cdot 10^{-4}$ A that is applied for 6 h (in accordance with the experimental setup in Johannisson et al. (2020)). As expected, the time evolution of $\bar{\Phi}^+(t)$ and $\bar{\Phi}^-(t)$ turn out to be identical (Fig. 6a). Fig. 6b shows schematically the evolution of the out-of-plane strain component (ϵ_{33}), which remain after the lithiation process is finished. Finally, Figs. 6c-d show how the Li-concentrations in the two electrodes (upper: $\hat{c}_{Li}^{f,+}$, lower: $\hat{c}_{Li}^{f,-}$) increase during the lithiation process. The Li-concentration is not completely uniform at the end of the prelithiation process. This is a result of transport limitations for the Li-ions, provided from the Li-metal electrodes on either sides of the respective fiber laminae (cf. Fig. 6a). It should be noted that, due to the symmetric design and idealized conditions, we obtain $\bar{\epsilon} \neq 0$ whereas $\bar{\kappa} = 0$.
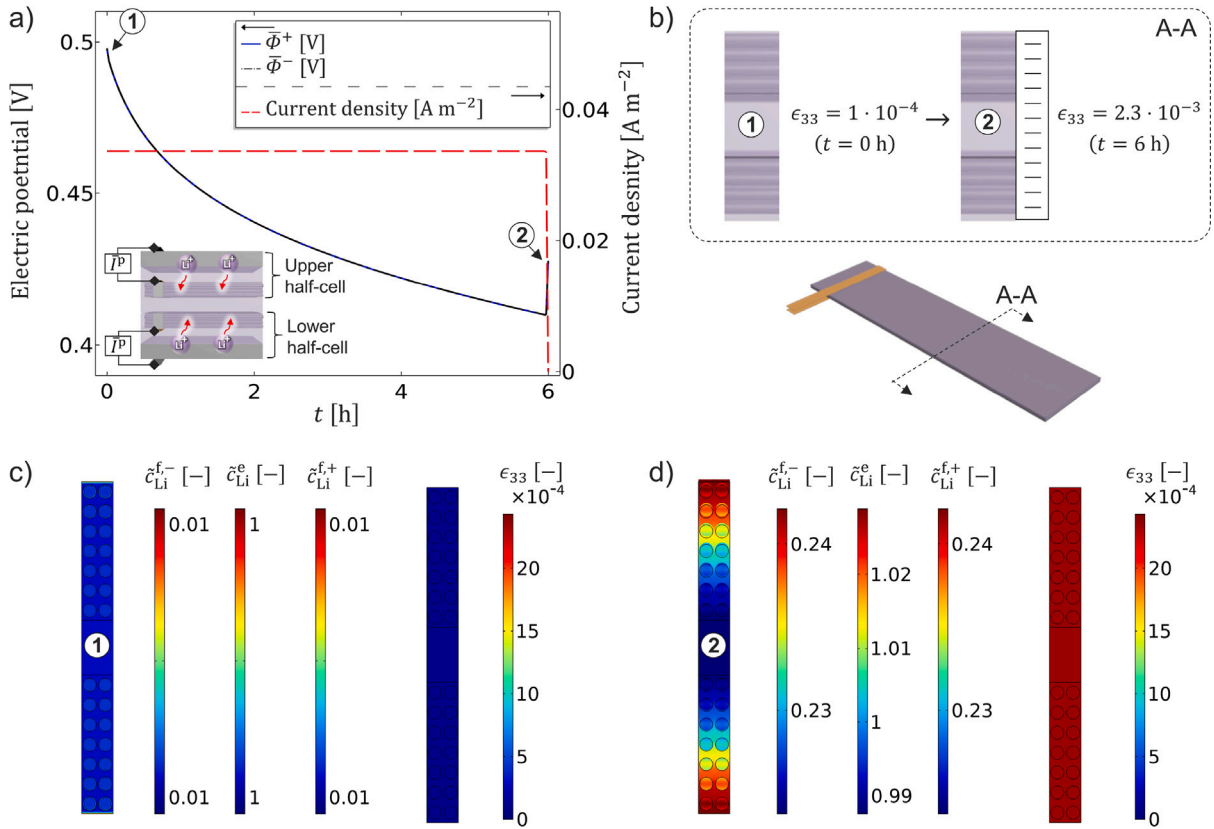
Fig. 6. Simulation of prelithiation of fibers "activation process" (total current of $\bar{I}^p = 5.9 \cdot 10^{-4}$ A, or a mass normalized current of 14.5 A kg^{-1} of fibers). (a) Electric potential of the two electrode half-cells (upper: $\bar{\Phi}^+$, lower: $\bar{\Phi}^-$) versus time during the lithiation process. (b) Schematic illustration showing the evolution of the out-of-plane strain component (ϵ_{33}) caused by the intercalation induced expansion of the fibers with increased Li-concentration at times ① $t = 0$ h, and ② $t = 6$ h, respectively. (c)–(d) The normalized Li-concentrations in the fibers in the upper ($\tilde{c}_{Li}^{f,+}$) and lower ($\tilde{c}_{Li}^{f,-}$) electrode, and the SBE ($\tilde{c}_{Li}^{e}$), and ϵ_{33} at the two times, respectively.

6.3. Sensor mode

In the sensor mode, the electric potential $\bar{\Phi}^+(t)$ is the sought response due to a prescribed (end) displacement $\bar{w}^p(t)$ of the beam. The start condition is defined by setting $\tilde{c}_{Li} = 0.23$ for both electrodes (cf. results attained in Section 6.2). The simulations are performed under "global" galvanostatic conditions, whereby a constant (small) total current of $\bar{I}^p = 1.7 \cdot 10^{-6}$ A is applied.[14] The current is set to a small value to imitate an electrical state of equilibrium. We note that it is also possible to use a zero-value current. The end deflection $\bar{w}^p(t)$ is conveniently parametrized as a "ramp-loading" in time during the interval $t \in [t_0, t_1]$ as follows:

$$\bar{w}^p(t) = \begin{cases} 0, & 0 \le t < t_0 \\ \bar{w}_0^p \frac{t - t_0}{t_1 - t_0}, & t_0 \le t < t_1 \end{cases} \tag{41}$$

Clearly, $\bar{w}_0^p$ is the magnitude of the prescribed end displacement.

The estimated shift in the difference of electric potential between the electrodes, $\bar{\Phi}^+ - \bar{\Phi}^-$, versus the prescribed end deflection, $\bar{w}^p$, is shown in Fig. 7a. The deformation mode of the beam for the two time instances ① (no mechanical load) and ② (forced bending downwards), are shown in Fig. 7b.

The computed voltage shift is confirmed qualitatively by experimental results of Harnden et al. (2022).

6.3.1. Load case: Constant curvature

To compare with experimental results in Harnden et al. (2022), we simulate a load case with constant curvature along the beam. The computed and experimental results for the electric potential difference (between the electrodes) as function of (constant) curvature are shown in Fig. 8. The experimental results are shown for both downward and upward bending for different curvatures (cf. Fig. 8 and Harnden et al. (2022)). A viable explanation for the difference in the experimental data between downward and

---

[14] The cross-sectional problem is solved under potentiostatic conditions while the "global" beam problem is solved under galvanostatic conditions.
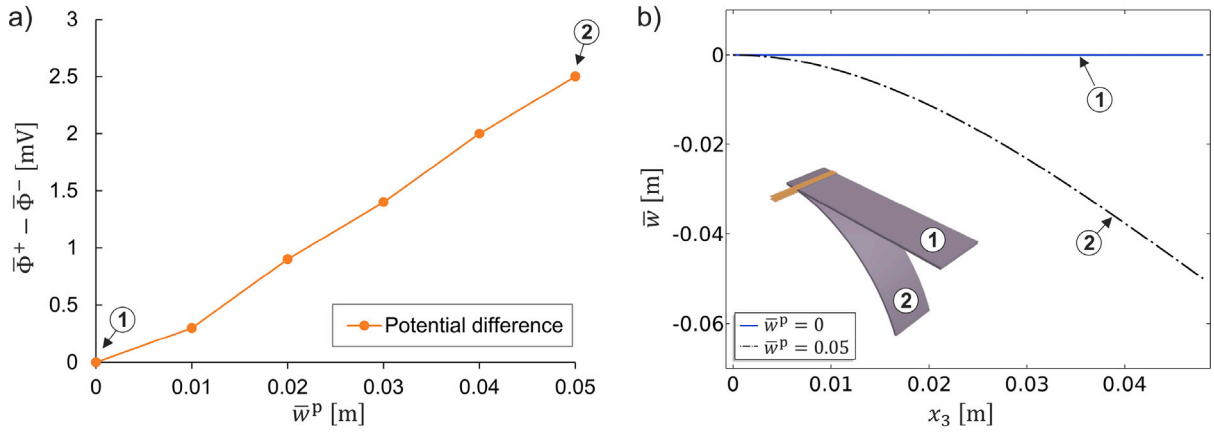
Fig. 7. Simulation of the sensor mode ($\bar{I}^p = 1.7 \cdot 10^{-6}$ A). (a) The electric potential difference between the electrodes versus the prescribed end deflection. (b) Displacement of the beam at the two instances ① (no mechanical load) and ② (forced bending downwards).
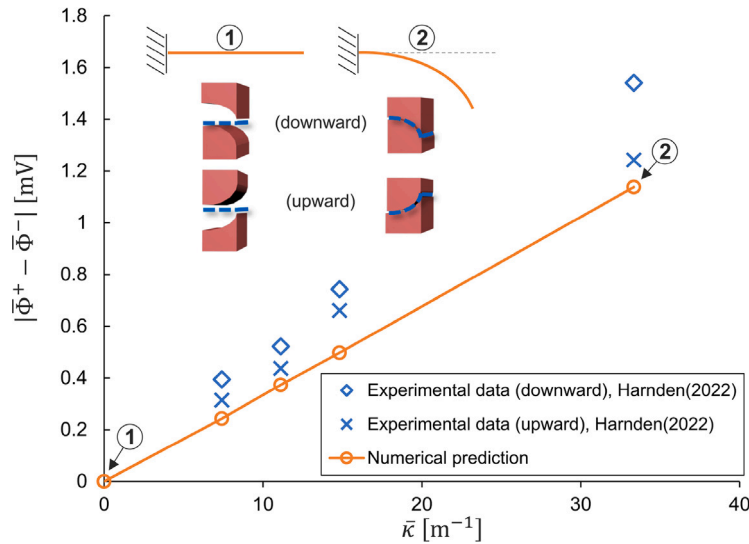

Fig. 8. Sensor problem: Predicted potential difference between the electrodes as function of applied (constant) curvature, compared to experimental data from Harnden et al. (2022). The experimental results are shown for both downward and upward bending for different curvatures.

upward bending is the observed slight difference in Li-concentration in the electrodes. For the numerical simulation, downwards and upwards deformation would give identical results due to symmetry. The agreement between experimental and numerical results is reasonable. For example, the experimental result shows a voltage response in the range of 1–1.2 mV for a curvature of $\bar{\kappa} = 33$ m^{-1}, which can be compared with the numerical prediction of approximately 1.14 mV.

6.4. Actuator mode

In the actuator mode, the end deflection $\bar{w}(L, t)$ becomes the response for a given constant total current $\bar{I}^p(t)$ supplied to the beam, representing galvanostatic control. As for the sensor mode, the start condition is defined by setting $\tilde{c}_{Li} = 0.23$ for both electrodes (cf. Section 6.2). A constant current of $\bar{I}^p = 5.9 \cdot 10^{-4}$ A is then applied for 5 h followed by a resting time of 1 h. A constant current in the opposite direction, i.e. $\bar{I}^p = -5.9 \cdot 10^{-4}$ A, is then applied for 10 h followed by another resting time of 1 h. The resulting potential difference (between the electrodes) and the end deflection are shown in Fig. 9a. Fig. 9b shows the bent beam at the states/times ①: $t = 0$ h, ②: $t = 5$ h, and ③: $t = 16$ h. We recall that the beam has zero curvature after (pre)lithiation, which represents the initial state for the actuation process. In Fig. 9c, the fields $\tilde{c}_{Li}(x_1, x_2)$ and $\epsilon_{33}(x_2)$ are shown for the time ②: $t = 5$ h. Apparently, the Li-ions have moved from the fibers in the lower electrode to the upper electrode, resulting in a downwards bent beam (cf. Fig. 9b). In Fig. 9d, the fields $\tilde{c}_{Li}$ and ϵ_{33} are shown at the time ③: $t = 16$ h. The Li-ions have now moved from the upper to the lower electrode, and the beam is bent upwards. Given the low magnitude of the out-of-plane strain component at the two time instances, we conclude that the assumption of small strains provides a reasonable estimate for the current loading conditions.
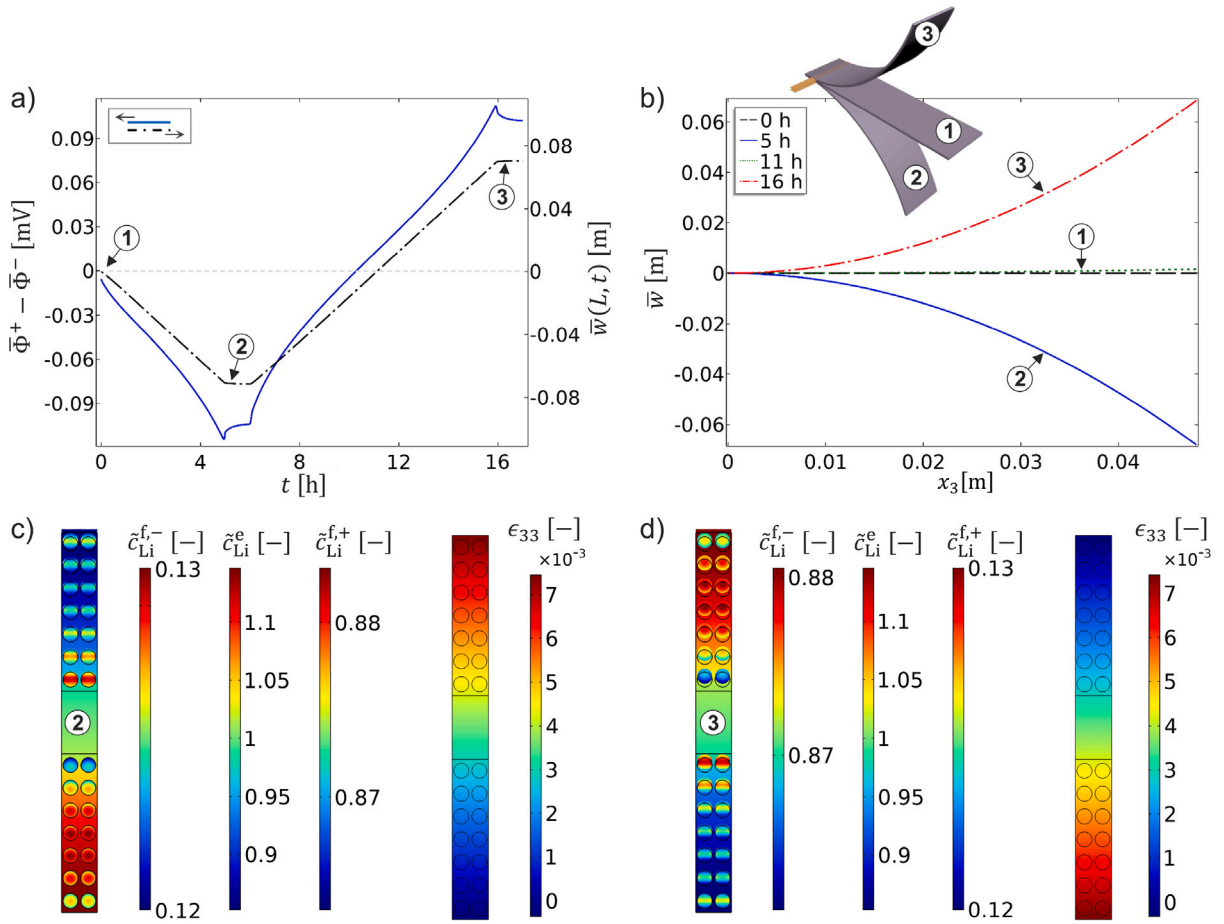
Fig. 9. Simulation of the actuator mode ($\bar{I}^p = 5.9 \cdot 10^{-4}$ A). (a) Potential difference and end deflection versus time. (b) Displacement of the beam at the times ①: $t = 0$ h, ②: $t = 5$ h, and ③: $t = 16$ h. (c)–(d) The normalized Li-concentrations (fibers $\tilde{c}^f_{Li}$ and electrolyte $\tilde{c}^e_{Li}$) and the out-of-plane strain component at times ②: $t = 5$ h and ③ $t = 16$ h, respectively.

We emphasize that linear beam kinematics is adopted in this paper, whereby the predicted deflection (denoted "linear" in Fig. 10) is found to be in good agreement with the experimental data only for quite limited deflections, Johannisson et al. (2020). Larger deflections however, are not well captured by the adopted linear beam model. A possible approach to improve the model is to account for moderately large deflections by utilizing the exact definition of curvature, i.e. $\bar{\kappa} = -\bar{w}'' \left[1 + (\bar{w}')^2\right]^{-3/2}$, in a post-processing step. In other words, when $\bar{\kappa}$ has been computed for the actuator problem in (38), then $\bar{w}$ can be computed (post-processed) from[15]

$$\bar{w}'' + \left[1 + (\bar{w}')^2\right]^{3/2} \bar{\kappa} = 0, \quad \bar{w}(0,t) = 0, \quad \bar{w}'(0,t) = 0 \tag{42}$$

The corresponding result is denoted "non-linear" in Fig. 10. It appears that the predicted end deflection is now quite close to the experimental data. We anticipate that the agreement would be even closer, had we used a model description accounting for truly large deformations. Furthermore, a possible source of discrepancy between experimental and numerical results is the observation by Johannisson et al. (2020) that the beam tip got in contact with the vertical wall (which the samples were mounted in) for large deflections. This effect was not accounted for in the computation. It is noted that the model parameters linked to e.g., geometric and material properties are set in accordance with Johannisson et al. (2020). In particular, the beam geometry (e.g., length and width) and the intercalation tensor α^{ch} are based on the given experimental data. No further parameter fitting was performed, demonstrating the accuracy of the developed model to predict the global response (beam deflection) when utilizing representative model parameters.

---

[15] This problem is solved in MATLAB by using the Euler method (ode45) for the pertinent first order system.
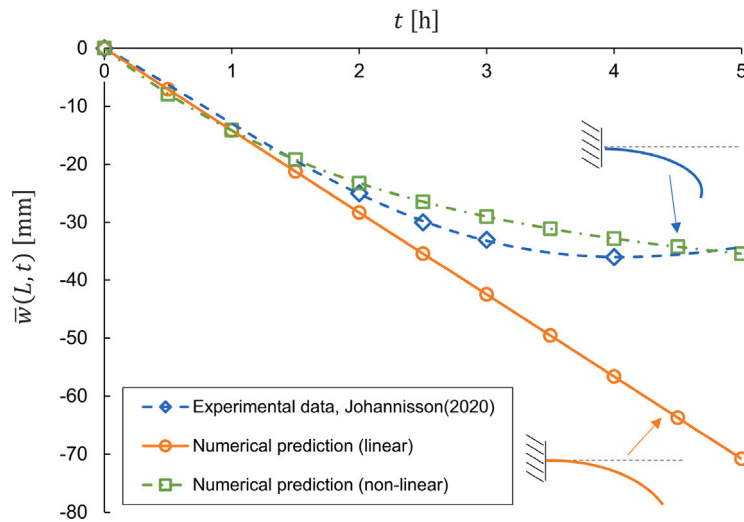
Fig. 10. Actuator problem: Predicted evolution of end deflection compared to experimental data from Johannisson et al. (2020).

7. Conclusions and outlook to future work

In this work, a computational modeling framework for a class of carbon fiber composites capable of shape-morphing and strain-sensing is developed. We build upon previous work by the authors, cf. Carlstedt et al. (2020), while extending the theory to allow for studying a beam composed of two (partly) lithiated carbon fiber electrodes on either side of a separator embedded in structural battery electrolyte (SBE). The sensor and actuator functionalities are achieved by the interplay between electrochemistry and mechanics, in particular the ability of carbon fibers to (de)intercalate Li-ions repeatedly. The numerical results show that the framework is capable of simulating both the actuator and sensor mode. In the case of actuation, the predicted deformation is found to be in close agreement with experimental data for small deflections. However for large deflections, geometric nonlinearities need to be accounted for. For the actuator mode it is found that large deflections of the beam can be captured via post-processing, whereby the exact definition of the curvature is utilized. Further, in the case of sensing, the voltage-strain coupling effect is predicted and the numerical results are found to agree with experimental data (Harnden et al., 2022). For the sensor mode, whenever the curvature along the beam is not constant, geometric non-linearities (or large rotations) of the beam need to be accounted for.

As for future work, it is necessary to account for truly large deformations, at least large rotations of the beam axis. This is clearly motivated by the comparison with experimental results for the actuator and sensor problems shown in Figs. 8 and 10. In terms of the dimensional split, such an extension can be combined with the restriction to small fluctuating deformations pertinent to the cross-sectional problem. However, relevant experimental data for validation, not only for the case of constant curvature along the beam, is currently lacking. Hence, performing such experiments is also an important part of future work. The influence of numerical errors should also be assessed, in particular from the mesh density in the beam versus the cross-sectional problem. A number of simplifying model assumptions have been introduced so far and should be validated. For example, it was assumed that the electric conductivity of fibers is very large so that the electric potential does not vary along the fibers. Further, viscous material behavior of the polymeric matrix should be accounted for. The extension to plate and shell action seems natural. Moreover, the current paper serves as the foundation for future studies. We foresee that the proposed technique of variationally consistent dimensional split can favorably be applied to full-cell structural batteries, cf. Asp et al. (2021), and structural energy harvesters, cf. Harnden et al. (2022). Hence, the developed framework can be used to study alternative load cases and applications, as well as different material designs.

CRediT authorship contribution statement

David Carlstedt: Conceptualization, Methodology, Software, Formal analysis, Visualization, Project administration, Funding acquisition, Writing – original draft. **Kenneth Runesson:** Conceptualization, Methodology, Supervision, Project administration, Funding acquisition, Writing – original draft. **Fredrik Larsson:** Conceptualization, Methodology, Supervision, Project administration, Writing – review & editing. **Ralf Jänicke:** Conceptualization, Methodology, Supervision, Project administration, Funding acquisition, Writing – review & editing. **Leif E. Asp:** Conceptualization, Methodology, Supervision, Project administration, Funding acquisition, Writing – review & editing.

Declaration of competing interest

The authors declare that they have no known competing financial interests or personal relationships that could have appeared to influence the work reported in this paper.

Table B.1

List of symbols.

Symbol	Unit	Description
φ	[V]	Electrical potential
μ_α	[J mol^{-1}]	Chemical potential of species α = Li,X
c_α	[mol kg^{-1}]	Ion concentration of species α = Li,X = molar bulk density of ions divided by bulk density
$\bar{c}_\alpha$	[–]	Normalized ion concentration of species α = Li,X
$\boldsymbol{\sigma}$	[Pa]	Stress tensor
$\mathbf{E}$	[Pa]	Elasticity tensor
$\boldsymbol{u}$	[m]	Displacement field tensor
ϵ	[–]	Strain tensor
ϵ^{ch}	[–]	Intercalation strain
$\boldsymbol{\alpha}^{\mathrm{ch}}$	[kg mol^{-1}]	Intercalation tensor
$\boldsymbol{j}_\alpha$	[mol m^{-2} s^{-1}]	Total ion flux vector of species α = Li,X
η_α	[m^{2}mol s^{-1} J^{-1}]	Mobility coefficient of species α = Li,X
$\boldsymbol{M}_\alpha$	[mol^2 m^{-1} s^{-1}J^{-1}]	Mobility tensor for species α = Li,X
$\mathcal{M}_{\mathrm{fe}}$	[mol^2 m^{-2} s^{-1} J^{-1}]	Interface mobility
$\mathcal{K}_{\mathrm{fe}}$	[S m^{-2}]	Interface ionic conductivity ($\mathcal{K}_{\mathrm{fe}} = F^2 M_{\mathrm{fe}}$)
$\mathcal{E}_{\mathrm{fe}}$	[F m^{-2}]	Interface permittivity
$\boldsymbol{i}$	[A m^{-2}]	Current density
$\boldsymbol{d}$	[C m^{-2}]	Electric flux density vector
θ	[K]	Temperature
ε	[F m^{-1}]	Permittivity
L	[Pa]; [m]	Lamé's first parameter; Length of beam
G	[Pa]	Shear modulus
$H_\parallel$	[Pa]	Uniaxial strain modulus
$\Phi^{+/-}$	[V]	Electrode potential: upper (+)/lower (–) electrode
$\bar{I}^{+/-}$	[A]	Total applied/prescribed current: upper (+)/lower (–) electrode
$\bar{s}^{+/-}$	[A]	"Current source", i.e. current entering the fiber via Li-ion transport from SBE
$\boldsymbol{t}$	[Pa]	Traction
t	[s]	Time
Ω	[–]	Domain
Γ	[–]	Boundary
ρ	[kg m^{-3}]	Density of carbon fiber
ρ^{F}	[kg m^{-3}]	Intrinsic density of fluid (electrolyte) in SBE
ϕ	[–]	Porosity
b	[–]	Bruggeman's constant
V_{f}	[–]	Fiber volume fraction
κ^{f}	[S m^{-1}]	Electric conductivity fibers
$\bar{w}$	[m]	Deflection (macroscale)
$\bar{\kappa}$	[m^{-1}]	Curvature (macroscale)
$\bar{M}$	[Nm]	Bending moment
$\bar{N}$	[N]	Normal force
$\bar{q}; \bar{f}; \bar{r}$	[N m^{-1}]; [N m^{-1}]; [N]	Loadings (mechanical)
h	[m]	Thickness of layer/lamina
w	[m]	Width
$\bar{\lambda}$	[–]	Lagrange multiplier

Data availability

Data will be made available on request.

Acknowledgments

Appendix A. Solution algorithm

The numerical implementation is done using the MATLAB-COMSOL LiveLink interface. Pseudocode for the MATLAB implementation (main program) is provided in Algorithm 1. The beam (1D) problem is solved using Newton iterations in accordance with Algorithm 1 in MATLAB, while the cross-sectional (2D) problem is solved using the Weak Form PDE module in COMSOL (at the Gauss points). The LiveLink interface is used to transfer data between the two types of software. The 1D beam is modeled using one beam element with two Gauss quatrature points, with linear shape functions for the

Table B.2
Material parameter values.

Parameter	Value	Unit	Description	Reference
$H_\parallel$	296	[GPa]	Uniaxial strain modulus fiber	Duan et al. (2020)
$L_\parallel$	5.5	[GPa]	Lamé's first parameter parallel fiber	Duan et al. (2020)
$L_\perp$	4.7	[GPa]	Lamé's first parameter perpendicular fiber	Duan et al. (2020)
$G_\parallel$	12.5	[GPa]	Shear modulus parallel (i.e. $x_3 - x_{1/2}$ plane) fiber	Duan et al. (2020)
$G_\perp$	9.4	[GPa]	Shear modulus perpendicular (i.e. $x_1 - x_2$ plane) fiber	Duan et al. (2020)
L^e	0.47	[GPa]	Lamé's first parameter SBE	Carlstedt et al. (2022c), Ihrner et al. (2017)
G^e	0.08	[GPa]	Shear modulus SBE	Carlstedt et al. (2022c), Ihrner et al. (2017)
L^{sep}	0.58	[GPa]	Lamé's first parameter separator phase	Johannisson et al. (2020)
G^{sep}	0.38	[GPa]	Shear modulus separator phase	Johannisson et al. (2020)
η_g^e	$8.1 \cdot 10^{-16}$	[m^2 mol s^{-1} J^{-1}]	Mobility of Li$^+$ and X$^-$ in SBE	Carlstedt et al. (2022c), Ihrner et al. (2017)
η_α^{sep}	$2.9 \cdot 10^{-16}$	[m^2 mol s^{-1} J^{-1}]	Mobility of Li$^+$ and X$^-$ in separator phase	–
η_{Li}	$5.8 \cdot 10^{-18}$	[m^{2}mol s^{-1} J^{-1}]	Mobility of Li in fiber (based on diffusion coefficient)	Kjell et al. (2013)
$\alpha_\perp^{ch}$	$3.5 \cdot 10^{-3}$	[kg mol^{-1}]	Transverse intercalation expansion coefficient	Johannisson et al. (2020), Jacques et al. (2013a)
$\alpha_\parallel^{ch}$	$7.1 \cdot 10^{-4}$	[kg mol^{-1}]	Longitudinal intercalation expansion coefficient	Johannisson et al. (2020), Jacques et al. (2013a)
$c_{Li,max}$	14	[mol kg^{-1}]	Maximum Li concentration in fiber	Johannisson et al. (2020), Jacques et al. (2013a)
$c_{\alpha,ref}$	0.14/1	[mol kg^{-1}]	Reference/initial concentration of Li in the fiber/Li$^+$ and X$^-$ in the SBE	Ihrner et al. (2017), Schneider et al. (2019)
ε_0	$8.854 \cdot 10^{-12}$	[F m^{-1}]	Vacuum permittivity	–
ε_r	10	[–]	Relative permittivity	Fontanella and Wintersgill (1988), Ganser et al. (2019)
$\mu_{Li,ref}$	$4.98 \cdot 10^4$	[J mol^{-1}]	Reference chemical potential Li in fiber (vs. Li/Li$^+$)	Kjell et al. (2013)
$\mu_{\alpha,ref}$	0	[J mol^{-1}]	Reference chemical potential Li$^+$ and X$^-$ in SBE	–
γ	1	[–]	Activity coefficient Li in fiber	–
ρ	1850	[kg m^{-3}]	Fiber density	–
ρ^F	1000	[kg m^{-3}]	Intrinsic density of fluid (electrolyte) in SBE	–
F	96485	[C mol^{-1}]	Faraday's constant	–
R	8.314	[J K^{-1} mol^{-1}]	Gas constant	–
θ_{ref}	293.15	[K]	Reference temperature (isothermal conditions)	–
L	0.048	[m]	Length of beam	Johannisson et al. (2020)
h_{beam}	$1.27 \cdot 10^{-4}$	[m]	Thickness of beam	Johannisson et al. (2020)
w_{beam}	0.02	[m]	Width of beam	Johannisson et al. (2020)
h_{ele}	$5.3 \cdot 10^{-5}$	[m]	Thickness of electrodes	Johannisson et al. (2020)
h_{sep}	$2.1 \cdot 10^{-5}$	[m]	Thickness of separator	Johannisson et al. (2020)
w_{ext}	$1.2 \cdot 10^{-5}$	[m]	Width of 2D-model unit	
V_f	0.43	[–]	fiber volume fraction (electrodes)	Johannisson et al. (2020)
ϕ^e/ϕ^{sep}	0.4/0.5	[–]	Porosity of the SBE/Separator	Ihrner et al. (2017), Johannisson et al. (2020)
b^e/b^{sep}	1.75/1.5	[–]	Bruggeman's constant for the SBE/Separator	Carlstedt et al. (2022c), Doyle et al. (1993)
$\mathcal{M}_{fe}$	$4.25 \cdot 10^{-9}$	[mol^2 m^{-2} s^{-1} J^{-1}]	Interface mobility	Carlstedt et al. (2022b)
$\mathcal{E}_{fe}$	0.18	[F m^{-2}]	Interface permittivity	Carlstedt et al. (2022b)

axial extension and cubic (Hermitian) shape functions for the deflection. The Jacobian is computed via numerical differentiation. To improve efficiency (in terms of required computational resources), the Jacobian is computed only for the first iteration at the first time step. Finally, the tolerance (for assumed convergence) TOL is set to a small value (here 10^{-8} was used).

Data: For given $\bar{I}^p$, $\bar{w}^p(t)$
Result: Solve for $\bar{\kappa}(t)$, $\bar{\varphi}^+(t)$
Set initial values of $\underline{z}^{(0)} = [\bar{\kappa}^{(0)}, \bar{\varphi}^{+,(0)}]$
for $t^{(n)} \to t_{end}$ **do**
    Time step: $t^{(n)} = t^{(n-1)} + \Delta t$
    Apply displacement: $\bar{w}^{p,(n)} = \bar{w}^p(t^{(n)})$
    while $|\underline{r}(\underline{z}^{(k)})| > TOL$ **do**
        Compute $\bar{s}^+$, $\bar{M}$ at Gauss points (COMSOL)
        Compute residual $\underline{r}^{(k)}$ using Gauss quadrature (MATLAB)
        if $t = t^{(1)}$ & $k = 1$ **then**
            Compute Jacobian: $\underline{J}^{(k)}$ (COMSOL)
        end
        Update: $\underline{z}^{(k+1)} = \underline{z}^{(k)} - [\underline{J}^{(k)}]^{-1}\underline{r}^{(k)}$
    end
end

Algorithm 1: Pseudocode for the implementation in MATLAB (main program).

Appendix B. Symbols and parameters

Symbols and parameters used in the analysis presented in this paper are listed in Tables B.1–B.2.

References

Arora, P., Zhengming, Z., 2004. Battery separators. Chem. Rev. 104, 4419–4462. http://dx.doi.org/10.1021/cr020738u.

Asp, L.E., Bouton, K., Carlstedt, D., Duan, S., Harnden, R., Johannisson, W., Johansen, M., Johansson, M., Lindbergh, G., Liu, F., Peuvot, K., Schneider, L.M., Xu, J., Zenkert, D., 2021. A structural battery and its multifunctional performance. Adv. Energy Sustain. Res. 2, 2000093. http://dx.doi.org/10.1002/aesr.202000093.

Bruggeman, D.A.G., 1937. Berechnung verschiedener physikalischer konstanten von heterogenen substanzen. III. Die elastischen konstanten der quasiisotropen mischkörper aus isotropen substanzen. Ann. Phys. 421, 160–178. http://dx.doi.org/10.1002/andp.19374210205.

Bucci, G., Swamy, T., Bishop, S., Sheldon, B.W., Chiang, Y.M., Carter, W.C., 2017. The effect of stress on battery-electrode capacity. J. Electrochem. Soc. 164, A645–A654. http://dx.doi.org/10.1149/2.0371704jes.

Carlstedt, D., Rittweger, F., Runesson, K., Navarro-Suárez, A.M., Xu, J., Duan, S., Larsson, F., Riemschneider, K.-R., Asp, L.E., 2022a. Experimental and computational characterization of carbon fibre based structural battery electrode laminae. Compos. Sci. Technol. 220, 109283. http://dx.doi.org/10.1016/j.compscitech.2022.109283.

Carlstedt, D., Runesson, K., Larsson, F., Asp, L.E., 2022b. On the coupled thermo-electro-chemo-mechanical performance of structural batteries with emphasis on thermal effects. Eur. J. Mech. A Solids 94, 104586. http://dx.doi.org/10.1016/j.euromechsol.2022.104586.

Carlstedt, D., Runesson, K., Larsson, F., Vinh, T., Jänicke, R., Asp, L.E., 2022c. Computational modelling of structural batteries accounting for stress-assisted convection in the electrolyte. Int. J. Solids Struct. 238, 111343. http://dx.doi.org/10.1016/j.ijsolstr.2021.111343.

Carlstedt, D., Runesson, K., Larsson, F., Xu, J., Asp, L.E., 2020. Electro-chemo-mechanically coupled computational modelling of structural batteries. Multifunct. Mater. 3, 045002. http://dx.doi.org/10.1088/2399-7532/abc60d.

Cha, Y., Porfiri, M., 2014. Mechanics and electrochemistry of ionic polymer metal composites. J. Mech. Phys. Solids 71, 156–178. http://dx.doi.org/10.1016/j.jmps.2014.07.006.

Chin, T.E., Rhyner, U., Koyama, Y., Hall, S.R., Chiang, Y.-M., 2006. Lithium rechargeable batteries as electromechanical actuators. Electrochem. Solid-State Lett. 9, A134. http://dx.doi.org/10.1149/1.2161523.

Doyle, M., Fuller, T.F., Newman, J., 1993. Modeling of galvanostatic charge and discharge of the lithium/polymer/insertion cell. J. Electrochem. Soc. 140, 1526. http://dx.doi.org/10.1149/1.2221597.

Duan, S., Liu, F., Pettersson, T., Creighton, C., Asp, L.E., 2020. Determination of transverse and shear moduli of single carbon fibres. Carbon 158, 772–782. http://dx.doi.org/10.1016/j.carbon.2019.11.054.

Fontanella, J.J., Wintersgill, M.C., 1988. Low frequency dielectric properties of polyether electrolytes. In: Polymer Electrolyte Reviews. Vol. 2. Elsevier Ltd.

Ganser, M., Hildebrand, F.E., Kamlah, M., McMeeking, R.M., 2019. A finite strain electro-chemo-mechanical theory for ion transport with application to binary solid electrolytes R. J. Mech. Phys. Solids 125, 681–713. http://dx.doi.org/10.1016/j.jmps.2019.01.004.

Grazioli, D., Magri, M., Salvadori, A., 2016. Computational modeling of Li-ion batteries. Comput. Mech. 58, 889–909. http://dx.doi.org/10.1007/s00466-016-1325-8.

Gupta, P., Gudmundson, P., 2021. A multi-scale model for simulation of electrochemically induced stresses on scales of active particles, electrode layers, and battery level in lithium-ion batteries. J. Power Sources 511, 230465. http://dx.doi.org/10.1016/j.jpowsour.2021.230465.

Harnden, R., Carlstedt, D., Zenkert, D., Lindbergh, G., 2022. Multifunctional carbon fibre composites: a structural, energy harvesting, strain-sensing material. ACS Appl. Mater. Interfaces 14, 33871–33880. http://dx.doi.org/10.1021/acsami.2c08375.

Harnden, R., Zenkert, D., Lindbergh, G., 2021. Potassium-insertion in polyacrylonitrile-based carbon fibres for multifunctional energy storage, morphing, and strain-sensing. Carbon 171, 671–680. http://dx.doi.org/10.1016/j.carbon.2020.09.042.

Ihrner, N., Johannisson, W., Sieland, F., Zenkert, D., Johansson, M., 2017. Structural lithium ion battery electrolytes: Via reaction induced phase-separation. J. Mater. Chem. A 5, 25652–25659. http://dx.doi.org/10.1039/C7TA04684G.

Jacques, E., Hellqvist Kjell, M., Zenkert, D., Lindbergh, G., Behm, M., 2013a. Expansion of carbon fibres induced by lithium intercalation for structural electrode applications. Carbon 59, 246–254. http://dx.doi.org/10.1016/j.carbon.2013.03.015.

Jacques, E., Kjell, M.H., Zenkert, D., Lindbergh, G., 2013b. Piezo-electrochemical effect in lithium-intercalated carbon fibres. Electrochem. Commun. 35, 65–67. http://dx.doi.org/10.1016/j.elecom.2013.07.040.

Johannisson, W., Harnden, R., Zenkert, D., Lindbergh, G., 2020. Shape-morphing carbon fiber composite using electrochemical actuation. Proc. Natl. Acad. Sci. 117, 7658–7664. http://dx.doi.org/10.1073/pnas.1921132117.

Kjell, M.H., Zavalis, T.G., Behm, M., Lindbergh, G., 2013. Electrochemical characterization of lithium intercalation processes of PAN-based carbon fibers in a microelectrode system. J. Electrochem. Soc. 160, A1473–A1481. http://dx.doi.org/10.1149/2.054309jes.

Larché, F.C., Cahn, J.W., 1973. A linear theory of thermochemical equilibrium of solids under stress. Acta Metall. 21, 1051–1063. http://dx.doi.org/10.1016/0001-6160(73)90021-7.

Latz, A., Zausch, J., 2013. Thermodynamic derivation of a Butler–Volmer model for intercalation in Li-ion batteries. Electrochim. Acta 110, 358–362. http://dx.doi.org/10.1016/j.electacta.2013.06.043.

Leronni, A., Bardella, L., 2021. Modeling actuation and sensing in ionic polymer metal composites by electrochemo-poromechanics. J. Mech. Phys. Solids 148, 104292. http://dx.doi.org/10.1016/j.jmps.2021.104292.

Newman, J., Thomas-Alyea, K.E., 2004. Electrochemical Systems. In: The ECS series of texts and monographs, Wiley.

Salvadori, A., Bosco, E., Grazioli, D., 2014. A computational homogenization approach for Li-ion battery cells: Part 1 - Formulation. J. Mech. Phys. Solids 65, 114–137. http://dx.doi.org/10.1016/j.jmps.2013.08.010.

Salvadori, A., Grazioli, D., Geers, M.G.D., 2015. Governing equations for a two-scale analysis of Li-ion battery cells. Int. J. Solids Struct. 59, 90–109. http://dx.doi.org/10.1016/j.ijsolstr.2015.01.014.

Schneider, L.M., Ihrner, N., Zenkert, D., Johansson, M., 2019. Bicontinuous electrolytes via thermally initiated polymerization for structural lithium ion batteries. ACS Appl. Energy Mater. 2, 4362–4369. http://dx.doi.org/10.1021/acsaem.9b00563.

Simo, J.C., Marsden, J.E., Krishnaprasad, P.S., 1988. The Hamiltonian structure of elasticity. The material and convective representation of solids, rods and plates. Arch. Ration. Mech. Anal. 104, 125–183. http://dx.doi.org/10.1007/BF00251673.

Xu, R., Yang, Y., Yin, F., Liu, P., Cloetens, P., Liu, Y., Lin, F., Zhao, K., 2019. Heterogeneous damage in Li-ion batteries: Experimental analysis and theoretical modeling. J. Mech. Phys. Solids 129, 160–183. http://dx.doi.org/10.1016/j.jmps.2019.05.003.

Zhang, X., Chumakov, S., Li, X., Klinsmann, M., Kim, S.U., Linder, C., Christensen, J., 2020. An electro-chemo-thermo-mechanical coupled three-dimensional computational framework for lithium-ion batteries. J. Electrochem. Soc. 167, 160542. http://dx.doi.org/10.1149/1945-7111/abd1f2.

Zhang, H., Grant, P.S., 2013. An electrochemical microactuator based on highly textured LiCoO2. Sensors Actuators B 176, 52–57. http://dx.doi.org/10.1016/j.snb.2012.08.079.

Zhuo, M., Grazioli, D., Simone, A., 2021. Tensorial effective transport properties of Li-ion battery separators elucidated by computational multiscale modeling. Electrochim. Acta 393, 139045. http://dx.doi.org/10.1016/j.electacta.2021.139045.